

# Massive sediment pulses triggered by a multi-stage 130,000 m<sup>3</sup> alpine cliff fall (Hochvogel, DE/AT)

Natalie Barbosa<sup>1,2</sup>, Johannes Leinauer<sup>2</sup>, Juilson Jubanski<sup>3</sup>, Michael Dietze<sup>4,5</sup>, Ulrich Münzer<sup>6</sup>, Florian Siegert<sup>1,3</sup>, Michael Krautblatter<sup>2</sup>.

- 5 <sup>1</sup>Department of Earth and Environmental Sciences, Faculty of Earth Sciences, GeoBio Center, Ludwig-Maximilians-University, Munich, 80333, Germany.  
<sup>2</sup>Chair of Landslide Research, Technical University of Munich, Munich, 80333, Germany  
<sup>3</sup>3D RealityMaps GmbH, Munich, 81673, Germany  
<sup>4</sup>Faculty of Geosciences and Geography, Georg-August-Universität Göttingen, Göttingen, 31073, Germany  
10 <sup>5</sup>GFZ German Research Centre for Geosciences, Potsdam, 14473, Germany  
<sup>6</sup>Department of Earth and Environmental Sciences, Section Geology, Ludwig-Maximilians-University, Munich, 80333, Germany.

*Correspondence to:* Natalie Barbosa ([barbosa@biologie.uni-muenchen.de](mailto:barbosa@biologie.uni-muenchen.de))

## 15 **Abstract**

Massive sediment pulses in catchments are a key alpine multi-risk component. Substantial sediment redistribution in alpine catchments frequently causes flooding, river erosion, and landsliding, and affects infrastructure such as dam reservoirs as well as aquatic ecosystems and water quality. While systematic rock slope failure inventories have been collected in several countries, the subsequent cascading sediment redistribution is virtually unaccessed.

20 This contribution reports for the first time the massive sediment redistribution triggered by the multi-stage failure of more than 130,000 m<sup>3</sup> from the Hochvogel dolomite peak during the summer of 2016. We applied change detection techniques on seven 3D-coregistered high-resolution true-orthophotos and digital surface models (DSM) obtained through digital aerial photogrammetry later optimized for precise volume calculation in steep terrain. The analysis of seismic information from surrounding stations revealed the temporal evolution of the cliff fall.

25 We identified the proportional contribution of >600 rockfall events (>1 m<sup>3</sup>) from 4 rock slope catchments with different slope aspects and their volume estimates. In a sediment cascade approach, we evaluated erosion, transport, and deposition from the rockface to the upper channelized erosive debris flow channel, then to the widened dispersive debris flow channel, and finally to the outlet into the braided sediment-supercharged Jochbach river. We observe the decadal flux of more than 400,000 m<sup>3</sup> of sediment, characterized by massive sediment waves

30 that (i) exhibit reaction times of 0-4 years in response to a cliff fall sediment input, and relaxation times beyond 10 years. The sediment waves (ii) manifest with faster response times of 0-2 years in the upper catchment and over 2 years in the lower catchments. The entire catchment (iii) undergoes a rapid shift from sedimentary (10<sup>2</sup>-10<sup>3</sup> mm/a) to massive erosive regimes (10<sup>2</sup> mm/a) within single years and the massive sediment redistribution (iv) shows limited dependency to rainfall frequency and intensity. This study provides generic information on spatial

35 and temporal patterns of massive sediment pulses in highly sediment-charged alpine catchments.

## **Keywords**

large format aerial photogrammetry, rockfall, massive sediment redistribution, increased debris flow activity, alpine catchment, Hochvogel.

## 1 Introduction

Recent high-magnitude rockfalls in the European Alps raised attention to the potential of catastrophic cascading sediment transport and their societal impact, e.g., Piz Cengalo Bergsturz (Baer et al., 2017). Sediment cascades define the dynamic process of sediment mobilization and deposition within a landscape that encompasses the continuous travel of sediment particles from their source, through the river network, and to eventual deposition in sediment sinks (Burt and Allison, 2010). Key driving processes to sediment cascades are landslides and rockfalls acting as sources of sediment, and debris flows and sediment transport as mechanisms of sediment remobilization. Several studies have focused on sediment cascades on active mountain environments controlled by landsliding (e.g., Benda and Dunne, 1997; Wichmann et al., 2009; Bennett et al., 2013; Heckmann et al., 2016; Clapuyt et al., 2019) as landslides provide and condition the input of sediment volumes into the sediment cascade (Benda and Dunne, 1997; Tucker, 2004). Attempts to better understand decadal to centennial erosion rates and sediment yield at a basin scale include geomorphological observations and spatial pattern analysis (Schrott et al., 2003; Theler et al., 2010), monitoring of sediment fluxes and construction of sediment budgets (Dietrich et al., 1982; Becht et al., 2009; Brown et al., 2009; Heckmann et al., 2016; Joyce et al., 2018), numerical modeling (Wichmann et al., 2009; Heckmann and Schwanghart, 2013; Bennett et al., 2014; Battista et al., 2022), and application of the connectivity framework (Borselli et al., 2008; Fryirs, 2013; Heckmann and Schwanghart, 2013; Bracken et al., 2015). These approaches incorporate both spatial and temporal variability in the operation of the sediment cascades at a diversity of scales, however, they lack key observations on rare and high-magnitude events and the subsequent sediment transfer at high spatial resolutions.

High-magnitude, low frequency events disrupt landscape dynamics, yielding a measurable time response. This response is the combination of the time required for a system to initiate a reaction, known as the reaction time, and the time taken for the system to complete the response and adjust to the change, referred to as the relaxation time. Debris flows are of particular societal concern (Owens et al., 2010) due to their short reaction times and long relaxation times expanding the temporal activity of the processes. Debris flows serve as a link to hillslope-channel coupling by connecting large parts of rock walls to the channel network (Heckmann and Schwanghart, 2013; Bennett et al., 2014). Debris flows rapidly mobilize  $< 10^2$  to  $>10^9$  m<sup>3</sup> of sediment (Jakob, 2005) along great distances reaching infrastructure and populated areas. While debris flows are typically considered transport-limited processes (Gregory and Lewin, 2014), numerical simulations suggest that continuous delivery of sediment from upslope areas to the location where debris flows are initiated maintains the supply of material available for transport, thus, impacting the persistence and magnitude of sediment pulses in the system (Heckmann and Schwanghart, 2013). Several studies have collected data from massive rock slope failures (e.g., Dussauge-Peisser et al., 2002; Heckmann et al., 2012; Fischer et al., 2012; Krautblatter et al., 2012; Guerin et al., 2020) which are a major landscape evolution process and significantly contribute to sediment yields by sporadic production of a considerable ( $<10^3$  m<sup>3</sup> km<sup>2</sup> yr<sup>-1</sup>) amount of debris (McSaveney, 2002; Korup et al., 2010; Krautblatter et al., 2012). In the coming decades with enhanced rainstorm activity, massive sediment redistribution primarily by debris flows in alpine catchments will be a key hazard and challenge in alpine communities, thus, constraining rates and sediment cascades response times to suddenly increased sediment input by landsliding is paramount for prediction and early warning.

Developments in digital photogrammetry allow the 3D reconstruction of landscapes from images taken by a diversity of platforms (Eltner and Sofia, 2020). Large format nadir-view digital photogrammetry with (multi-)year temporal resolution and high-spatial resolution (20 cm) covering vast areas, presents a valuable, yet unexplored, data source for quantification of geomorphic changes in the last decade despite their challenges (Fawcett et al., 2019). Photogrammetric models of steep terrain and pseudo-vertical walls include random errors still difficult to minimize and quantify accurately, yet allow the unlock of a historical perspective and provide insights on sediment cascade spatial patterns in climate-sensitive landscapes (e.g., Fabris and Pesci, 2009; Berger et al., 2011; Bennett et al., 2012; Savi et al., 2023). Despite the temporal resolution that results in the coalescence of events, a combination of techniques such as high-resolution seismic investigation provides a potential complement to the photogrammetric record. Environmental seismology uses the seismic signals emitted by earth's surface processes to track back their origin (Dietze et al., 2017).

This paper reports the massive sediment redistribution triggered by the multi-stage failure from the Hochvogel dolomite peak during the summer of 2016. We evaluate the spatio-temporal morphodynamics at a catchment scale before and after the cliff fall by means of multi-temporal high-resolution aerial photogrammetry between 2010 and 2020. The (multi-) annual photogrammetric surveys provide information on detachment areas and failed volumes. Still, the temporal resolution is limited to the recurrence interval between two consecutive surveys, i.e., one to two years. Thereby, we intend to decipher rockfall patterns and catchment sediment dynamics after an unusual sediment input to the catchment. Additionally, we complement the understanding of a multi-stage single rockfall event by the use of high-resolution seismic records (e.g., Hibert et al., 2011; Lacroix and Helmstetter, 2011; Manconi et al., 2016; Fuchs et al., 2018; Dietze et al., 2017a). The combination of seismic information with high-resolution wide-extent photogrammetric reconstructions resulted in (i) identification of the spatial and temporal contribution of rockfall material from the four rock slope catchments that constitute the Hochvogel summit, (ii) quantification of (multi-) annual series of sediment budgets erosion rates before and after the cliff fall evidencing the dramatic inversion of deposition and erosion processes, (iii) time series of sediment cascading and (iv) estimation of the system reaction time and redistribution controls with respect to rainstorm intensity and frequencies. To our knowledge, this paper is one of few publications showing the cascading sediment response of an alpine catchment to a massive rock slope failure. This enables a better understanding of short-, mid- and long-term catchment morphodynamic responses to high magnitude rock fall, propagation, and persistence of sediment waves through alpine catchment system and future hazard scenarios where increased sediment availability and seasonal extreme heavy rainfall are expected.

## 2 Study area

The Hochvogel peak (47°21'N, 10°26'E, 2,592 m a.s.l), is a prominent summit in the Northern Calcareous Alps and a popular destination for hikers. The Hochvogel massif consists of Hauptdolomit, a brittle, variably bituminous carbonate rock with pronounced bedding (dm-m) and incidental marly interlayers. The rock mass is tectonically stressed and highly weathered. A meter-size fracture at the summit poses a catastrophic rock failure scenario (Leinauer et al., 2020, 2021) directly impacting the Weittal valley (Figure 1).

120

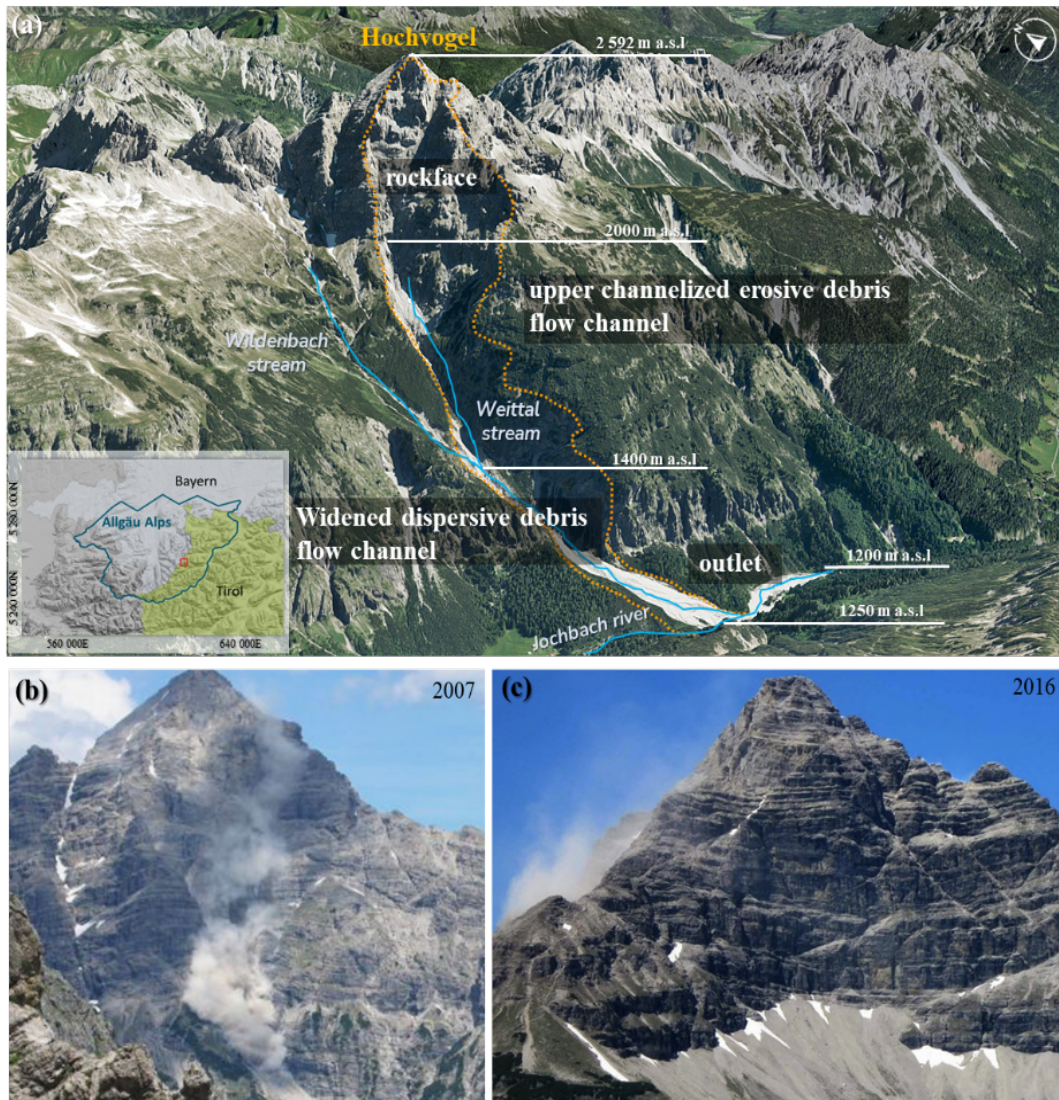
Four slopes constitute the pyramidal-shaped summit with orientations towards northeast, west, southeast, and southwest and mean inclinations between 43° to 47°. The southwestern slope is distinguished by its current almost vertical wall and upper negative slope reaching the peak of the summit. Slope processes occurring at the southwestern slope are transferred to the Weittal catchment which extends over 1.9 km<sup>2</sup> with an elevation  
125 difference of more than 1,300 m. The area directly affected by slope instabilities occurring at the southwestern slope covers 378,642 m<sup>2</sup> between 2010 to 2021 and is divided into four morpho-dynamic zones (Figure 1a) **rock face**: with strong slope changes, serve as the source of sediment production (primary and secondary rockfalls), **upper channelized erosive debris flow channel**: characterized by a mean slope of 42°, promotes temporal accumulation of sediment in an incipient slope talus. A confined asymmetric valley follows the slope talus limited  
130 to the east by vertical walls of almost 60 m in height. At the same time, to the west, sporadic minor pulses of sediment are produced by erosion of the base of an older slope deposit gently oriented southwest. **widened dispersive debris flow channel**: geographically limited by the intersection of the Weittal and Wildenbach streams, starts by a rock wall confined valley which transforms into a highly active unconfined slope under continuous incision of older deposits and the **outlet** into the Jochbach river which imposes a high sediment transfer  
135 regime evidenced in the braided development of the river along an alluvial plain with a mean inclination of 14° and the presence of terraces with a height between 1 to 3 m from the current main channel.

Rockfalls on the southeastern and southwest slopes of the Hochvogel summit were documented in 1934, 1935, 2005, and 2007 (DAV, 2017). Between Saturday 9 and Monday 11 of July 2016 (Heißel and Figl, 2017), noises  
140 and a dust cloud alerted the local authorities due to a new rockfall event that affected the Weittal valley (Figure 1. b and c.).

### 3. Methods

#### 3.1 Multi-temporal quantification of surface change

We used large format aerial imagery surveyed by the Austrian and German Cartographic Survey offices (BEV &  
145 LDBV) and by 3D RealityMaps GmbH to investigate the spatial and temporal sediment production, transport, and accumulation patterns of the southwest slope of the Hochvogel in 6 intervals over ten years. All seven surveys (09.2010, 08.2012, 09.2014, 06.2015, 08.2017, 09.2018, and 08.2020) have a nominal 20 cm spatial resolution (supplementary Table 1.) for the production of the digital surface models (DSM) and true orthophotos from the photogrammetric point clouds. The produced DSMs were aligned to the reference dataset acquired on 21.09.2018  
150 by means of a 3D-coregistration for the further application of change detection and volume calculation.



155 **Figure 1. a) Location of the Hochvogel summit in the Allgäu Alps between Bavaria (Germany) and Tirol (Austria) and 3D-reconstruction of the southwest slope indicating the approximate elevation of the boundaries of the morphodynamic zones: rockface, upper channelized erosive debris flow channel, widened dispersive debris flow channel, and outlet. The orange dotted line delimits the 378,642 m<sup>2</sup> impacted by the cliff fall studied in this contribution. b) Dust cloud over the southwest slope produced by the 2007 rockfall event (DAV, 2017) b) southeastern slope with remnant dust cloud from the 2016 rockfall event at the southwest slope (DAV, 2016).**

### 3.1.1 2.5D topographic time series

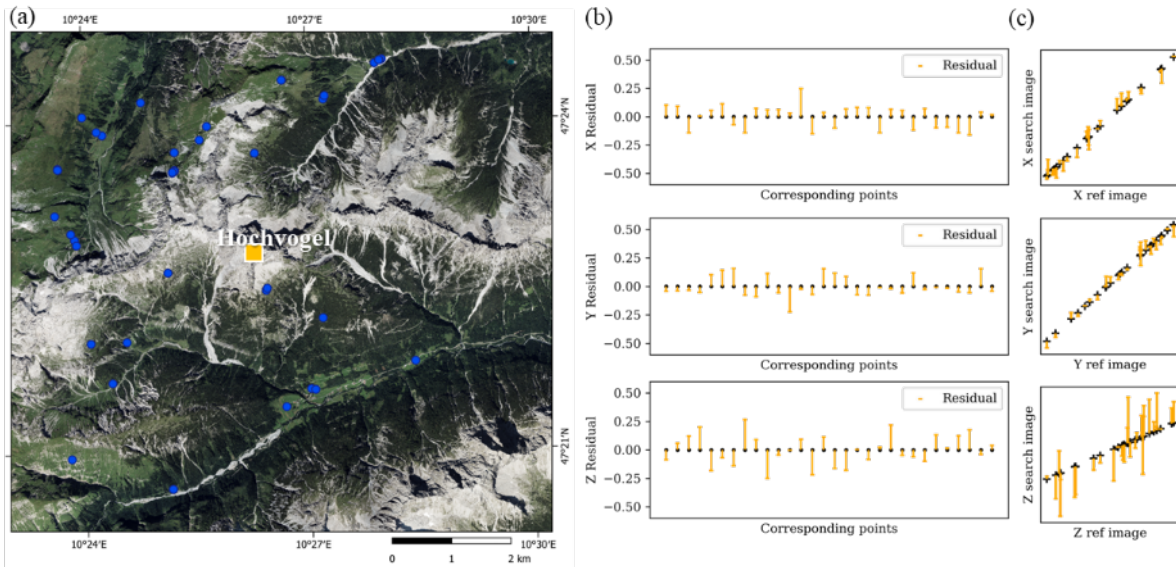
160 The photogrammetric workflow to generate DSM and true orthophoto from nadir view aircraft photographs consist of the initial standardization of the aerotriangulation provided by the survey agencies into the same spatial reference system using the software Inpho and Match-AT by Trimble, and followed by the generation of oriented point clouds, DSM, and orthophotos using the semi-global matching algorithm first developed by (Hirschmüller, 2008) and implemented in the software SURE from nFrames (ESRI) (Haala and Rothermel, 2012; Rothermel et al., 2012). The DSM follows the same grid from the orthophoto, but only high-quality elevation points identified by a multi-triangulation of at least 3 photographs are written in the non-interpolated DSM. We optimized the orthophotos and non-interpolated DSMs for a more precise volumetric calculation in steep terrain by the application of a 7-parameter 3D similarity transformation described by (Eq. (1)). To minimize the 3D distance between a reference dataset (DSM and Orthophoto) (21.09.2018) and the interest datasets, we manually selected

165

170 30 multi-temporal well-distributed 3D corresponding points  $(x, y, z)$  located in stable, non-changeable areas using the true orthophotos and the corresponding DSMs, and solved Eq. (1) using the least-squares adjustment solution in python:

$$\begin{bmatrix} x_{obs} \\ y_{obs} \\ z_{obs} \end{bmatrix} = \lambda \begin{bmatrix} \cos(\varphi)\cos(\kappa) & \sin(\omega)\sin(\varphi)\cos(\kappa) - \cos(\omega)\sin(\kappa) & \cos(\omega)\sin(\varphi)\cos(\kappa) + \sin(\omega)\sin(\kappa) \\ \cos(\varphi)\sin(\kappa) & s \in (\omega)\sin(\varphi)\sin(\kappa) + \cos(\omega)\cos(\kappa) & \cos(\omega)\sin(\varphi)\sin(\kappa) + \sin(\omega)\cos(\kappa) \\ -\sin(\varphi) & s \in (\omega)\cos(\varphi) & \cos(\omega)\cos(\varphi) \end{bmatrix} \begin{bmatrix} x_{ref} - x_0 \\ y_{ref} - y_0 \\ z_{ref} - z_0 \end{bmatrix} \quad (1)$$

where  $[x_{obs}, y_{obs}, z_{obs}]^T$  and  $[x_{ref}, y_{ref}, z_{ref}]^T$  are the vectors of coordinates of the corresponding points at the interest dataset  $s(x, y, z)$  and reference dataset  $r(x, y, z)$  with size  $(1, 3 * n_{corresponding\ points})$  respectively ;  $\lambda$  is the uniform scale factor;  $[x_0, y_0, z_0]^T$  is the vector of approximate values of the parameters; and  $\omega, \varphi, \kappa$  represent the rotation Euler Angles used to calculate the orthogonal rotation matrix  $M$ ,  $m_{ij} = M(\omega, \varphi, \kappa)$ . Parameters  $\lambda$  and  $[x_0, y_0, z_0]^T$  are initially approximated to 0 and  $M(\omega, \varphi, \kappa)$  to  $\frac{\pi}{180}$ . The evaluation of the estimated parameters  $M(\omega, \varphi, \kappa)$ ,  $\lambda$  and  $[x_0, y_0, z_0]^T$  after the convergence of the model (5 iterations) results in the elimination of outliers and the warranty of randomness in the residual values defined as the difference between the  $r(x, y, z)$  and  $s_{trans}(x, y, z)$ , being  $s_{trans}$  the new coordinates of the corresponding points at the search surface after the application of the transformation parameters (Figure 2).



185 **Figure 2. a) True orthophoto of the reference surface acquired on 21.09.2018. Blue dots indicated the corresponding points with the search surface acquired on 07.08.2017. Similar spatial distribution is followed for the remaining datasets according to the extent of the acquisition. b) Residuals calculated as the difference between the  $r(x, y, z)$  and  $s_{trans}(x, y, z)$ , being  $s_{trans}$  the new coordinates of the corresponding points at the search surface after the application of the transformation parameters for each spatial axis x, y, and z. c) Spatial distribution of the corresponding points at each spatial axis x, y, and z.**

190 Repetitive topographic surveys, in our case DSMs, allow the identification and quantification of geomorphic changes such as erosion and deposition. We followed the guidelines given by James et al. (2012) and Wheaton et al. (2010) for the estimation of area and volume of change based on 2.5D data., i.e., rasterized topography following Eq. (2):

$$DoD = Z_{new} - Z_{old} \quad (1)$$

195

where DoD is the difference of elevation between consecutive DSMs ( $Z_{new}$  and  $Z_{old}$ ). Despite the limited depiction of vertical walls and possible artifacts for overhanging walls, gridded datasets, i.e., DSM, support the fast and straightforward calculation of 2.5 D volumes by Eq. (3):

200

$$V = a \sum_{i=1}^n DoD_i \quad (3)$$

$$\text{where } a = n * a_{pixel} \quad (4)$$

and  $n$  is the number of pixels conceding with a meaningful change, i.e., pixels over or under a critical threshold,  $a_{pixel}$  corresponds to  $0.4 \text{ m}^2$ , and  $DoD_i$  is the elevation difference between time periods.

205

We used the non-interpolated DSMs to minimize the change to noise ratio (Wheaton et al., 2010; Anderson, 2019). Elevation uncertainty of photogrammetric surveys is roughly assessed as three times the spatial resolution, however, lighting conditions, surface roughness, and camera configuration among others, imprint an inhomogeneous spatially distributed uncertainty that remains challenging to estimate. Thus, we evaluated the uncertainty of the elevation change ( $\delta_{DoD}$ ) after the 3D-coregistration using 30 independent well-distributed points on stable areas with complex topography for each DoD independently (supplementary Table 2). The uncertainty of the elevation change ( $\delta_{DoD}$ ) is measured as the Root mean square error (RMSE) of the elevation difference in stable areas with complex topography and ranges between 30 to 40 cm (supplementary Table 3). We segmented the study area into four regions based on morphometric characteristics (Figure 1), to acknowledge the role of topography on elevation uncertainty. Hereby slope angle and slope aspect, influence the minimum detectable change through time but also imprint morphodynamic characteristics (Sect. 2.). Conservative critical thresholds above the measured coregistration error and elevation uncertainty for each region were determined by best practice between 0.2 to 1 m (supplementary Table 4 and 5). Selecting these critical threshold values influences the calculation of rockfall magnitude and sediment transport volumes. However, they will not affect the rockfall patterns and the response of sediment dynamics in terms of reaction and relaxation times.

210

215

220

We filter the different sources of topographic changes by semi-automatic filtering, and final manual inspection using 3D visualization. The filtering processes focus on the identification of ‘false’ rockfalls, defined as elongated polygons in the z component in relation to their horizontal area generated due to poor edge depiction. First, we segmented the DoD using a 3x3 circular kernel on a binary mask of change (1)-no change (0) defined by the critical thresholds. The size of the kernel was selected to segment an approximate connected change of a minimum of  $1 \text{ m}^2$ . We used descriptive statistical information from each polygon: minimum and maximum elevation change, area of change, volume of change, and mean slope before the change, to filter the polygons using the criteria described in Table 1. The slopes at the Hochvogel are mostly highly-fractured and horizontally layer, thus, rock falls preferentially follow a pseudo-cubic form. A 3D visualization supports the final visual inspection.

225

230

235

**Table 1. Attributes, argumentation, and threshold value used to filter the change polygons from noise. Threshold values are selected by visual inspection of the filtering results. (A) rockface, (B) Upper channelized erosive debris flow channel, (C) Widened dispersive debris flow channel, and (D) outlet.**

Attribute	Usage	Threshold value
Area/Maximum elevation change	Detection and elimination of vertical changes that correspond to poor edge depiction.	< 1
Mean slope before the change	Differentiation of erosion and deposition area based on physical parameters.	Erosion at (A) and (B) is limited to slopes with > 30° Erosion at (C) occurred on slopes > 5°  Deposition at (A), (B) and (C) is limited by the repose angle of calcareous materials approximated to < 50°
Number of pixels of change	Detection of small changes which are prone to higher uncertainty and visually inconclusive.	<15 connected pixels

240

The 3D-coregistration process suggest a neglectable horizontal error at the pixel level, thus, the total volume uncertainty ( $\delta V$ ) from Eq (3) is the sum of the uncertainty of each cell of volume ( $\delta v$ ). The cell of volume  $v$  is calculated such Eq (5):

$$v = a_{pixel} D o D_{pixel} \quad (5)$$

245 To propagate the errors of each cell of volume, the partial derivative of Eq (5) with respect to the elevation change, which is the variable that has uncertainty, is calculated:

$$\delta v = |v'(D o D)| \delta_{D o D} \quad (6)$$

$$\text{where } \delta_{D o D} = RMSE_{Z_{time\ period}}$$

Finally, the volume uncertainty over area A is given by Eq. (7):

250

$$\delta V = A \delta v \quad (7)$$

255 The proposed workflow for the calculation of volumes of changes in steep terrain using large format high-resolution aerial imagery results from the combination of previously published methodologies and the implementation of intermediate steps that responds to the particularities of the datasets. A summary of the methodological step is presented in Figure 1 supplementary material.

### 3.1.2 Frequency-magnitude curves

A frequency-magnitude curve relates the magnitude of a variable to the frequency of occurrence (Riggs, 1968). The curve is an estimate of the incremental yearly cumulative frequencies from the largest magnitude event to the smallest (Hungt et al., 2008). We included both primary and secondary rockfalls in our analysis. We acknowledge the occurrence of coalescent events, given the (multi-) yearly temporal resolution of the datasets (Williams et al., 260 2019), however, we do not intend to resolve single rockfalls but we aim to decipher the relative rockfall activity in the last decade for each of the rockface slopes that constitute the summit (Dussauge-Peisser et al., 2002; Benjamin et al., 2020; Hantz et al., 2021). We assessed the volumetric errors due to the steep topography by the



iterative calculation of the volume of a known event (2016 cliff fall) using all possible combinations of DSMs  
265 (Table 6 supplementary material).

### 3.1.3 Cascading geomorphic sediment budgets

A sediment budget describes the input, transport, storage, and export of sediment in a geomorphic system. This  
270 concept provides an effective basis for representing the key components of the sediment delivery system within a  
catchment and for assembling the necessary data to elucidate, understand and predict catchment sediment delivery  
(Walling and Collins, 2008) and estimate related natural hazards. The geomorphic sediment budget (Wheaton et  
al., 2010) is calculated as the sum of the masked DoD values of erosion (negative change) and deposition (positive  
change).

275

We calculate the proportion of net erosion and net deposition per year ( $\text{m}^3 \text{y}^{-1}$ ) based on the number of days  
between acquisitions, comparable to previous studies. Conversion to mass (t) is based on reported densities of  
limestone  $2.6 \text{ t m}^3$  and limestone deposits  $2 \text{ t m}^3$  according to (Krautblatter et al., 2012). Spatially averaged short-  
term wall retreat rates were calculated by dividing the total rockfall volume per year ( $\text{m}^3 \text{y}^{-1}$ ) by the area over  
280 which the volumes were calculated., i.e., northern slope ( $253,643 \text{ m}^2$ ), western slope ( $115,098 \text{ m}^2$ ), southwestern  
slope ( $254,686 \text{ m}^2$ ), southeaster slope ( $165,037 \text{ m}^2$ ), rockface ( $234,329 \text{ m}^3$ ), upper channelized erosive debris flow  
channel ( $53,072 \text{ m}^3$ ), widened dispersive debris flow channel ( $91,241 \text{ m}^3$ ) and outlet ( $34,004 \text{ m}^3$ ).

## 3.2. Volume estimation of the 2016 multi-event

### 3.2.1. 3D cumulative volume

285 The 2016 rockfall dramatically changed the morphology of the southwestern slope of the Hochvogel (Figure 3).  
We calculated the total rockfall volume using the most complete photogrammetric point clouds derived from the  
large format aerial imagery before the event, 23.09.2014, and after the event, 07.08.2017. We manually delimited  
the extent of the 2016 rockfall event based on the cloud-to-cloud distance algorithm in CloudCompare v2.0. The  
volume calculation was performed over a grid of 0.2 cm and an average height cell in CloudCompare v2.0. For  
290 visualization purposes, we reconstructed the detached surface by creating a mesh using the Poisson Surface  
Reconstruction plugin (Kazhdan et al., 2020) and the two-point clouds. The approximate orientation of fractures  
was extracted from the photogrammetric point cloud 23.09.2014 using the CloudCompare plugin Compass  
(Thiele et al., 2017).

### 3.2.2. Multi-stage detachment analysis

295 For the time interval in which the 2016 failure occurred (July 9 to 11), we downloaded all available seismic data  
from seven surrounding broadband stations (distance to Hochvogel: 12-55 km) (supplementary table 7). By  
analyzing the local seismic amplitude and the corresponding spectrograms at each station, we identified all seismic  
events with the strongest impact at the closest station in Oberstdorf. Rock falls produce a seismic impact over all  
frequencies between 5 and 50 Hz (Dietze et al., 2017; Le Roy et al., 2019); in our case, we expect a clear decrease  
300 in seismic intensity with increasing distance of the stations from the Hochvogel and significant arrival time  
differences of up to 20 s (Figure 4 supplementary material). On the contrary, earthquakes often show distinct

arrivals of P and S waves, a lower frequency content, and smaller arrival time differences. Local anthropogenic noise is characterized by higher frequency contents and missing coincidence of the signal between different stations. Following these criteria, we identified all potential seismic signals originating from the rock fall series  
305 at the Hochvogel.

Despite significant variability in the scaling of  $E_p$  to  $E_s$  (cf. (Hibert et al., 2011), Le Roy et al. (2019) determined a relation between generated seismic energy  $E_s$  and the potential energy of a rock fall  $E_p$  such:

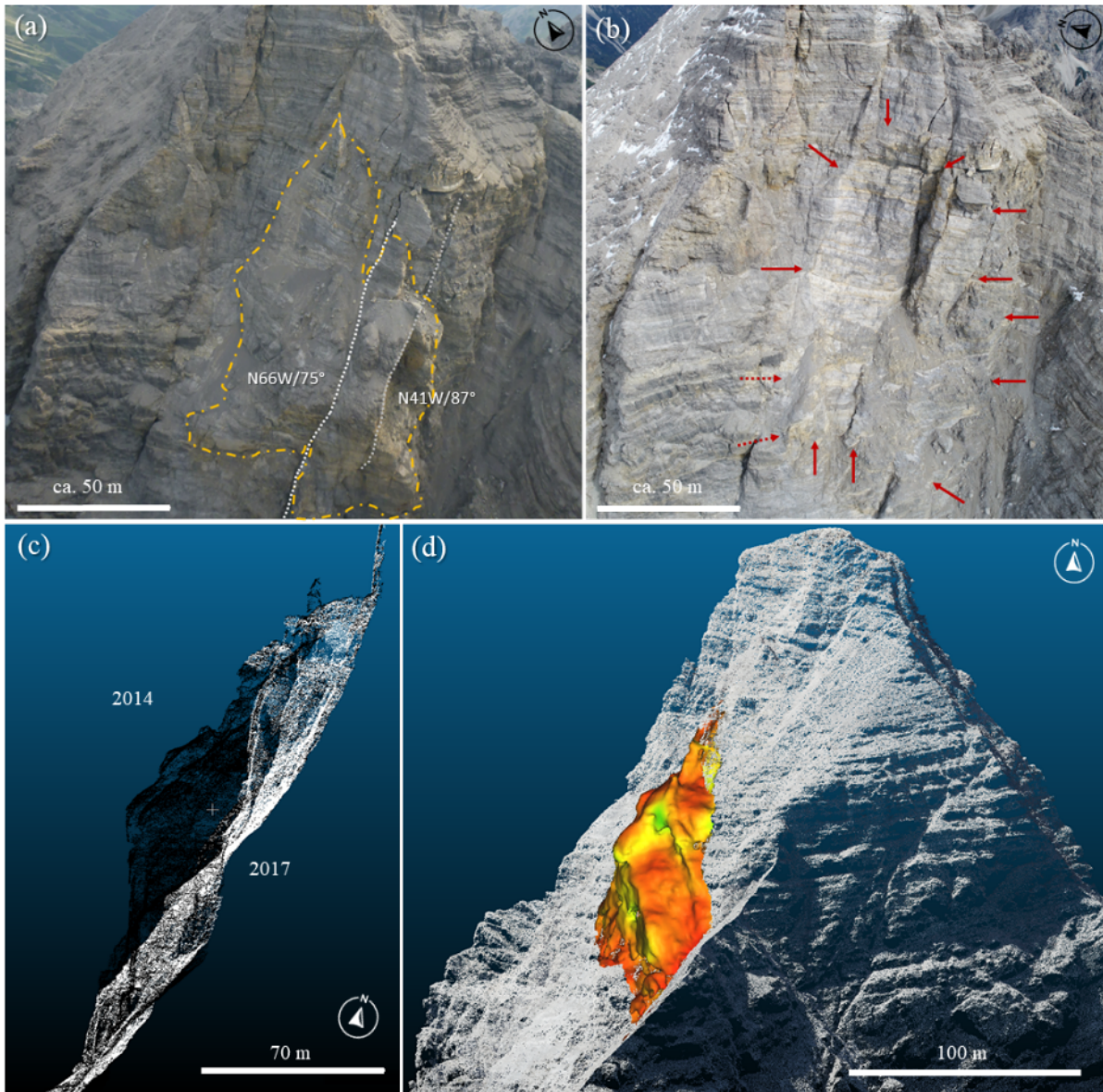
$$E_s = 10^{-8} \times E_p^{1.55} \quad (11)$$

310 The initially failed volume can then be derived from the potential energy if we determine the fall height of the block that generated the seismic signal. We estimated the fall height of the rock fall event from the photogrammetric point cloud differences and 3D models. A simple toppling of the center of gravity towards the slope corresponds to a fall height of 50-60 m while a sliding of the failed block suggests a probable fall height of 75 to 100 m. The calculation of the seismic energy and the determination of all needed parameters mainly follows  
315 the methodology in Le Roy et al. (2019) (supplementary Sec. 2). We estimated the error of the calculations based on Monte Carlo simulations with 1000 iterations and the variability of the different stations.

## 4. Results

### 4.1 Multi-stage occurrence of the 2016 cliff fall event

320 The cliff fall that occurred during the summer of 2016 resulted in the detachment of  $1.31 (\pm 0.01) \cdot 10^5 \text{ m}^3$  of dolomite following a multi-stage development. The extent of the cliff detachment is indicated by the clearer color tone on the rock surface (Figure 3b.), and the detachment area was measured to be  $4,777 \text{ m}^2$  using a combination of the best photogrammetric derived point clouds before and after the cliff fall. Prior to the cliff fall, the area was characterized by a vertical rock tower surrounded by pervasive fractures with orientation NW and pseudo-vertical  
325 dip angles that may have contributed to the multi-stage detachment by widening preexisting rock discontinuities (Figure 3a). The rock tower had a height exceeding 60 meters and was a prominent feature in the landscape. Currently, partially disconnected blocks are limited by penetrative fractures and represent areas of potential detachments. The cliff fall resulted in a significant change in the morphology of the southwest slope increasing the mean slope by  $1^\circ$  from  $45.6^\circ$  to  $46.6^\circ$ .



330

335

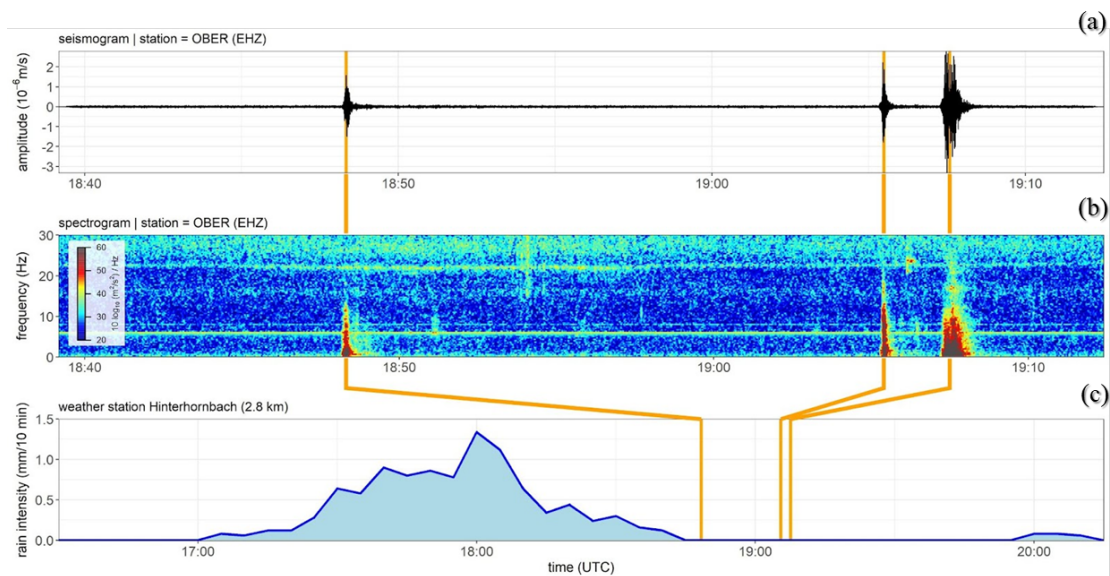
Figure 3. Picture taken by Land Tyrol during a helicopter flight inspection before the cliff fall (03.07.2015). The yellow line indicates the cliff fall detachment area in the summer of 2016. The fracture orientations (in white) intend to exemplify approximate structure orientation and must be taken with caution due to the low point density in the exposed fracture surfaces. b) Picture taken by TUM Landslides group (Andreas Dietrich) after the cliff fall (28.09.2017) using an Unmanned aerial vehicle (UAV) - DJI Phantom 4 during a monitoring survey as part of the AlpSenseBench project on 28.09.2017. The red arrows indicate the cliff fall detachment area in the summer of 2016 c) Photogrammetric point clouds from the surveys on 23.09.2014 in black and 07.08.2017 in white. d) Mesh reconstruction of the cliff fall.

The seismic signal analysis indicates a progressive failure of the total mass in at least three to six portions within 3 days (Table 2). The biggest parts of the rock mass failed on the last day (2016.07.11) at 20:48, 21:05, and 21:07 local time. The volume estimation from the seismic energy at the closest station in Oberstdorf (OBER) results in a median volume of  $1.02 (\pm 0.09) \cdot 10^5 \text{ m}^3$  for a fall height of 60 m. The estimated volume excludes smaller rockfalls, since the limited energy released by these events may not be recorded by the seismic stations. As a result, the seismically estimated volume may underestimate the total amount of material detached.

345

**Table 2. Temporal multiphase cliff fall detachment between July 9th and 11th 2016 at the Oberstdorf station (OBER). Detected event phases and partial volumes (given as median  $\pm$  sd).**

Event	First arrival time at OBER in UTC	Status	Mean volume from station OBER with fall height = 60 m [m <sup>3</sup> ]
1	2016-07-09 08:37:45	probably rock fall signal	8.92 ( $\pm$ 1.52) *10 <sup>3</sup>
2	2016-07-09 17:39:27	probably rock fall signal	1.96 ( $\pm$ 0.32) *10 <sup>3</sup>
3	2016-07-11 17:39:36	probably rock fall signal	2.83 ( $\pm$ 0.54) *10 <sup>3</sup>
4	2016-07-11 18:48:13	clearly rock fall signal	1.74 ( $\pm$ 0.30) *10 <sup>4</sup>
5	2016-07-11 19:05:19	clearly rock fall signal	1.83 ( $\pm$ 0.32) *10 <sup>4</sup>
6	2016-07-11 19:07:16	clearly rock fall signal	5.25 ( $\pm$ 0.88) *10 <sup>4</sup>
SUM			1.02 ( $\pm$ 0.09) *10 <sup>5</sup>



350 **Figure 4. Unmistakable rock detachments on 11th July at the Oberstdorf seismic station (OBER) a) Amplitude of the seismic signal b) spectrogram covering all frequencies up to 30 Hz. c) rainfall intensity at Hinterhornbach (mm/10 min) before and after the rock detachments.**

#### 4.2 Summit slope erosion

Over the last decade, the Hochvogel summit has produced 1.713 ( $\pm$ 0.04) \*10<sup>5</sup> m<sup>3</sup> of sediment, corresponding to  
355 an annual production rate of 43,990 ( $\pm$  1 069) t y<sup>-1</sup> when assuming a rock density of 2 600 kg m<sup>-3</sup> (Krautblatter et al., 2012). Notably, 97% of this sediment can be attributed to the 2016 cliff fall at the Southwestern slope. A total of 667 erosional events, including primary and secondary rockfalls, were detected at the Hochvogel summit, with a median volume ranging between 4.6 to 9.3 m<sup>3</sup>. The minimum detectable rockfall volume ranged between 1.4 to 2.1 m<sup>3</sup>, depending on the slope orientation. The sediment production on the four slopes of the summit showed a  
360 significant disproportion. The western and southeastern slopes had the lowest rockfall frequency, while the northern slope experienced the highest rockfall activity per year (Figure 5). However, when considering the contribution of rockfall magnitudes following the volumetric classification based on Whalley (1974, 1984);

Erismann and Abele (2001); Krautblatter et al. (2012), debris falls dominate the northern and western slopes, while the southeaster slope has a larger proportion of boulder fall, accounting for 55% of the total contribution (Table 3).

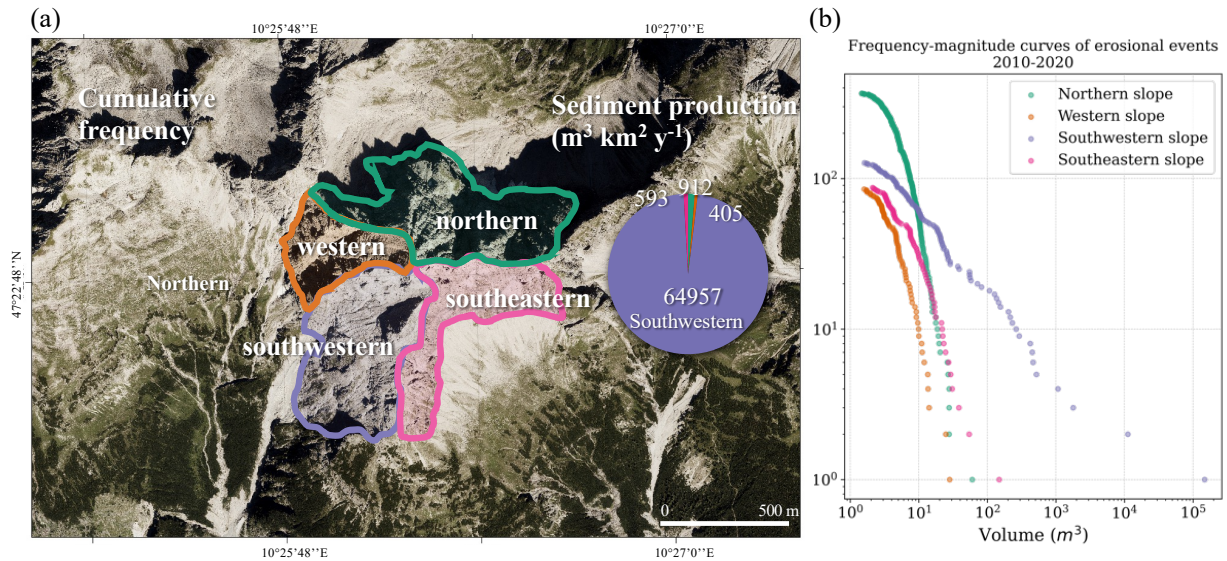


Figure 5. Erosional events between 2010 and 2020. i.e., primary and secondary rockfalls grouped by slope orientation. a) slope orientation, cumulative frequency per slope, and sediment production per year. b) Frequency-volume curves for the 667 erosional events on a logarithmic scale.

370 Table 3. Contribution of rockfall magnitudes. Volumetric classification based on Whalley, (1974, 1984); Erismann and Abele (2001); Krautblatter et al. (2012). \* Error equal to total volume percentage error of 2.4% (Table 6 supplementary material). Rockwall retreat refers to the horizontal retreat of the vertical rock cliff.

	northern slope 253 643 m <sup>2</sup>		western slope 115 098 m <sup>2</sup>		southwestern slope 254 686 m <sup>2</sup>		southeastern slope 165 037 m <sup>2</sup>		Total (m <sup>3</sup> )
	Total (m <sup>3</sup> )	(%)	Total (m <sup>3</sup> )	(%)	Total (m <sup>3</sup> )	(%)	Total (m <sup>3</sup> )	(%)	
<b>Debris fall</b> Volume < 10 m <sup>3</sup>	1.53 (±0.03) * 10 <sup>3</sup>	65	3.34 (±0.08) * 10 <sup>2</sup>	71	3.37 (±0.08) * 10 <sup>2</sup>	0	3.01 (±0.07) * 10 <sup>2</sup>	30	2.50 (±0.06) * 10 <sup>3</sup>
<b>Boulder fall</b> 10 < Volume < 10 <sup>2</sup> m <sup>3</sup>	8.11 (±0.20) * 10 <sup>2</sup>	35	1.38 (±0.03) * 10 <sup>2</sup>	29	1.07 (±0.02) * 10 <sup>3</sup>	1	5.41 (±0.13) * 10 <sup>2</sup>	55	2.56 (±0.06) * 10 <sup>3</sup>
<b>Block fall</b> 10 <sup>2</sup> < Volume < 10 <sup>4</sup> m <sup>3</sup>	0	0	0	0	6.57 (±0.16) * 10 <sup>3</sup>	4	1.48 (±0.04) * 10 <sup>2</sup>	15	6.72 (±0.16) * 10 <sup>3</sup>
<b>Cliff fall</b> 10 <sup>4</sup> < Volume < 10 <sup>6</sup> m <sup>3</sup>	0	0	0	0	1.59 (±0.03) * 10 <sup>5</sup>	95	0	0	1.59 (±0.03) * 10 <sup>5</sup>
<b>Total volume (m<sup>3</sup>)</b>	2.34 (±0.05) * 10 <sup>3</sup>		4.72 (±0.011) * 10 <sup>2</sup>		1.67 (±0.04) * 10 <sup>5</sup>		9.90 (±0.24) * 10 <sup>2</sup>		1.71 (±0.04) * 10 <sup>5</sup>
<b>Volume per year</b> (m <sup>3</sup> y <sup>-1</sup> )*	2.31 (±0.06) * 10 <sup>2</sup>		4.6 (±0.10) * 10 <sup>1</sup>		1.65 (±0.04) * 10 <sup>4</sup>		9.7 (±0.20) * 10 <sup>1</sup>		1.69 (±0.04) * 10 <sup>4</sup>
<b>Rockwall retreat</b> (mm y <sup>-1</sup> )	<b>0.9</b>		<b>0.4</b>		<b>64</b>		<b>0.5</b>		

### 4.3. Geomorphic sediment budget

375 The short-term denudation rates in the catchment prior to the cliff fall were 45 to 52 mm y<sup>-1</sup>, resulting in a negative catchment sediment budget ranging -1.29 (±0.02) \* 10<sup>4</sup> m<sup>3</sup> y<sup>-1</sup> and -1.59 (±0.04) \* 10<sup>4</sup> m<sup>3</sup> y<sup>-1</sup>. Following the cliff

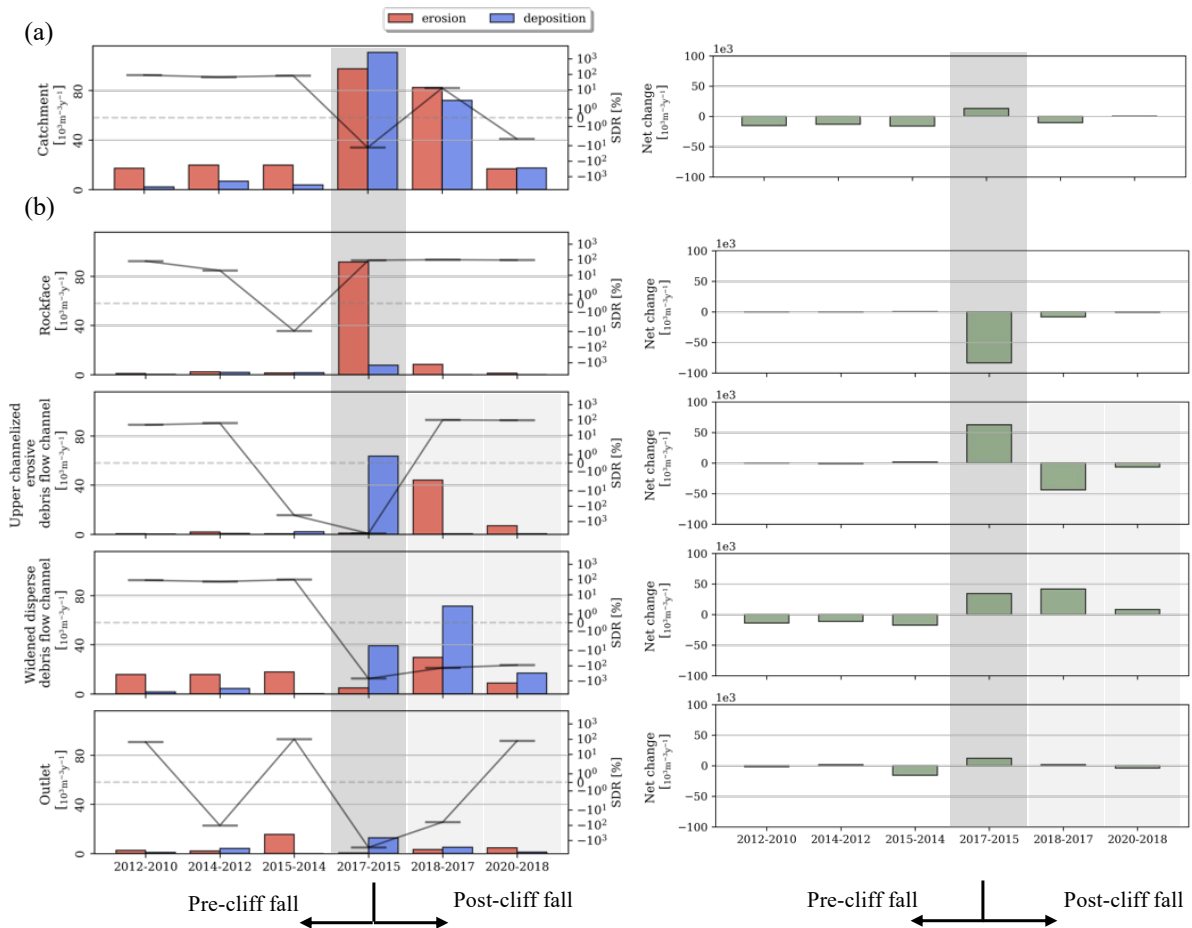
fall, the catchment's denudation rates increased abruptly by ten times, reaching 257 mm y<sup>-1</sup>. Despite the erosion of 9.74 (±0.01) \*10<sup>4</sup> m<sup>3</sup> y<sup>-1</sup>, the sediment delivery to the outlet was significantly reduced, resulting in a positive catchment sediment budget of 1.30 (±0.06) \*10<sup>4</sup> m<sup>3</sup> y<sup>-1</sup> (Figure 6a). Two years after the event, within catchment sediment waves dominated the sediment flow to the outlet leading to a negative sediment budget of -1.03 (±0.08) \*10<sup>4</sup> m<sup>3</sup> y<sup>-1</sup>. Subsequently, a slightly positive sediment budget of 6.12 (±2) \*10<sup>2</sup> m<sup>3</sup> y<sup>-1</sup> evidenced the ongoing sediment redistribution within the catchment four years after the cliff fall, even though, the catchment denudation rates returned to pre-event levels of 44 mm y<sup>-1</sup>. Catchment scale erosion and deposition volumes at each time interval are listed in Table 4.

385 **Table 4. Catchment scale erosion, deposition and net volumes (m<sup>3</sup>). Catchment denudation rates (mm y<sup>-1</sup>) were calculated based on the affected area extend (378,642 m<sup>2</sup>). The volume uncertainty is calculated independently for each single interval and process, i.e., erosion and deposition. \* Error propagated from erosion and deposition uncertainties (Table 6 supplementary material).**

Interval	Erosion		Deposition		Net change	
	Volume (m <sup>3</sup> )	Rates (mm y <sup>-1</sup> )	Volume (m <sup>3</sup> )	Rates (mm y <sup>-1</sup> )	Volume (m <sup>3</sup> )	Volume* (m <sup>3</sup> y <sup>-1</sup> )
2010-2012	3.40 (±0.02) *10 <sup>4</sup>	45	4.237 (±0.006) *10 <sup>4</sup>	5	-2.97 (±0.03) *10 <sup>4</sup>	-1.51 (±0.01) *10 <sup>4</sup>
2012-2014	4.20 (±0.02) *10 <sup>4</sup>	52	1.45 (±0.01) *10 <sup>4</sup>	18	-2.75 (±0.04) *10 <sup>4</sup>	-1.29 (±0.02) *10 <sup>4</sup>
2014-2015	1.54 (±0.03) *10 <sup>4</sup>	52	2.99 (±0.002) *10 <sup>4</sup>	10	-1.24 (±0.03) *10 <sup>4</sup>	-1.59 (±0.04) *10 <sup>4</sup>
2015-2017	2.08 (±0.002) *10 <sup>5</sup>	257	2.36 (±0.01) *10 <sup>5</sup>	291	2.78 (±0.13) *10 <sup>4</sup>	1.30 (±0.06) *10 <sup>4</sup>
2017-2018	9.38 (±0.04) *10 <sup>4</sup>	217	8.20 (±0.04) *10 <sup>4</sup>	189	-1.18 (±0.09) *10 <sup>4</sup>	-1.03 (±0.08) *10 <sup>4</sup>
2018-2020	3.33 (±0.02) *10 <sup>4</sup>	44	3.46 (±0.01) *10 <sup>4</sup>	46	1.21 (±0.43) *10 <sup>3</sup>	6.12 (±2) *10 <sup>2</sup>

#### 390 4.4. Geomorphic sediment budgets across the sediment cascade

The differentiated geomorphic sediment budgets (Figure 6b) and time series of spatial distribution of differences of DSMs (Figure 7) reveals the fast system response to the cliff fall. The concept of sediment continuity refers to the transfer or exchange of sediment across various parts of the hillslope system, which involves the conservation of mass among sediment inputs, stores and output (Joyce et al., 2018). Sediment storages and sinks (marked as 395 (1), (2), (3), and (4) in Figure7) define the boundaries between different morphodynamic zones, which are characterized by slight changes in mean slope that imprints morphological controls on transport processes. Regardless of the existence of depositional landforms, sediment continuity dominates from 2010 until 2014 evidenced in negative net change at all the geomorphic system zones.



400 **Figure 6. Time series of geomorphic sediment budgets. a) Geomorphic sediment budgets at the catchment scale. b)**  
 405 **segregated sediment budget into the four morphodynamic zones. Left column: The bar plot depicts yearly volumes of erosion in red and deposition in blue (units at the left axis). The black line indicates the sediment delivery ratio expressed as the proportion of sediment leaving the morphodynamic zone from the total net erosion (units at the right axis). Right column: yearly net change calculated as the difference between erosion and deposition. The estimated uncertainty of the absolute volume is less than 2% thus, imperceptible due to the scale of the graph. Dark grey polygons highlight the temporal stamp at which the cliffs fall took place. Lighter grey indicates the system response two and four years after the event. Note how the reverse net changes propagate downslope the system through time.**

An initial disruption in the sediment continuity is observed between 2014 and 2015. At the rockface, boulder and block falls occur, which detach from the sub-vertical wall and deposit at its base. Additionally, in the upper  
 410 channelized erosive debris flow channel, less than  $< 10^2 \text{ m}^3$  of recently deposited material (less than two years of residence time) are internally redistributed. However, even during this period of localized disruption, sediment redistribution continues to take place at the widened debris flow channel, which ensures sediment delivery to the outlet into the braided sediment-supercharged Jochbach river (Figure 7).

415 Following the cliff fall event, there was an immediate disruption of sediment transfer among the different morphodynamic zones, with about 75% of the produced sediment being deposited at the upper channelized erosive debris flow channel (Figure 6b. 2017-2015). A total of  $1.356 (\pm 0.003) * 10^5 \text{ m}^3$  of sediment were deposited over the 1.5 km length of the upper channelized erosive debris flow channel. Despite the positive sediment budget at the widened disperse debris flow channel, massive deposition occurred at the outlet. The bi-yearly temporal  
 420 resolution masks the highly dynamic sediment transport, however, the formation of a terrace of almost 3 m evidence the deposition of at least  $2.60 (\pm 0.03) * 10^4 \text{ m}^3$  after the cliff fall. Field evidence suggests the infill of the

outlet flood plain with new debris that impacted the dynamics of the riverbed (Figure 3 supplementary material). The pre-event channel of the Jochbach river is filled with up to 4 m of material in its deeper part at the end of 2017, one year after the cliff fall (Figure 7, morphodynamic zone D). The infill results in a migration of the channel  
425 to the center of the Outlet flood plain marked by a discontinuous erosional area in Figure 7 for 2017-2018, and finally the formation of a main channel towards the north, evident in Figure 7 by the continuous erosional pattern for the time interval between 2018 and 2020.

A dramatic inversion from deposition to erosion occurs two years after the cliff fall. Sediment waves or slugs  
430 deposited  $8.14 (\pm 0.04) * 10^4 \text{ m}^3$  at the apex of the widened dispersive debris flow channel infilling the valley with 3 m of transported material which increased to almost 10 m four years after the cliff fall (Figure 7 and Figure 9, profile C-C'). Despite the increased sediment input due to the cliff fall, there were reversed net changes between the widened dispersive debris flow channel and outlet four years after the cliff fall (Figure 6, 2018-2020).

## 435 **5. Discussion**

The (multi-) annual high resolution aerial imagery datasets provide an insightful look on sediment cascades at a decadal scale. Despite the coalesce of events due to the temporal resolution, the revealed patterns of sediment redistribution and geomorphic response time caused by the increased sediment input due to a cliff fall (Owens et  
440 al., 2010) are highly relevant for the assessment of cascading risks. The proposed 3D-coregistration workflow optimizes the DSMs extracted from consecutive nadir view large format aerial surveys for volumetric calculations of rockfall and sediment erosion and deposition volumes in steep terrain. However, there are still limitations on the representation of complex topography. Thus, it requires careful thought about the validity of the measurements. Despite this, the presented results are paramount to identifying and better understanding coupling  
445 mechanisms of high-magnitude slope events at a high temporal-spatial resolution to the fluvial system at a catchment scale. The analysis of within hillslope morphodynamics and its coupling with the fluvial system exemplify the alpine catchment response to future climatic changes and landscape dynamics.

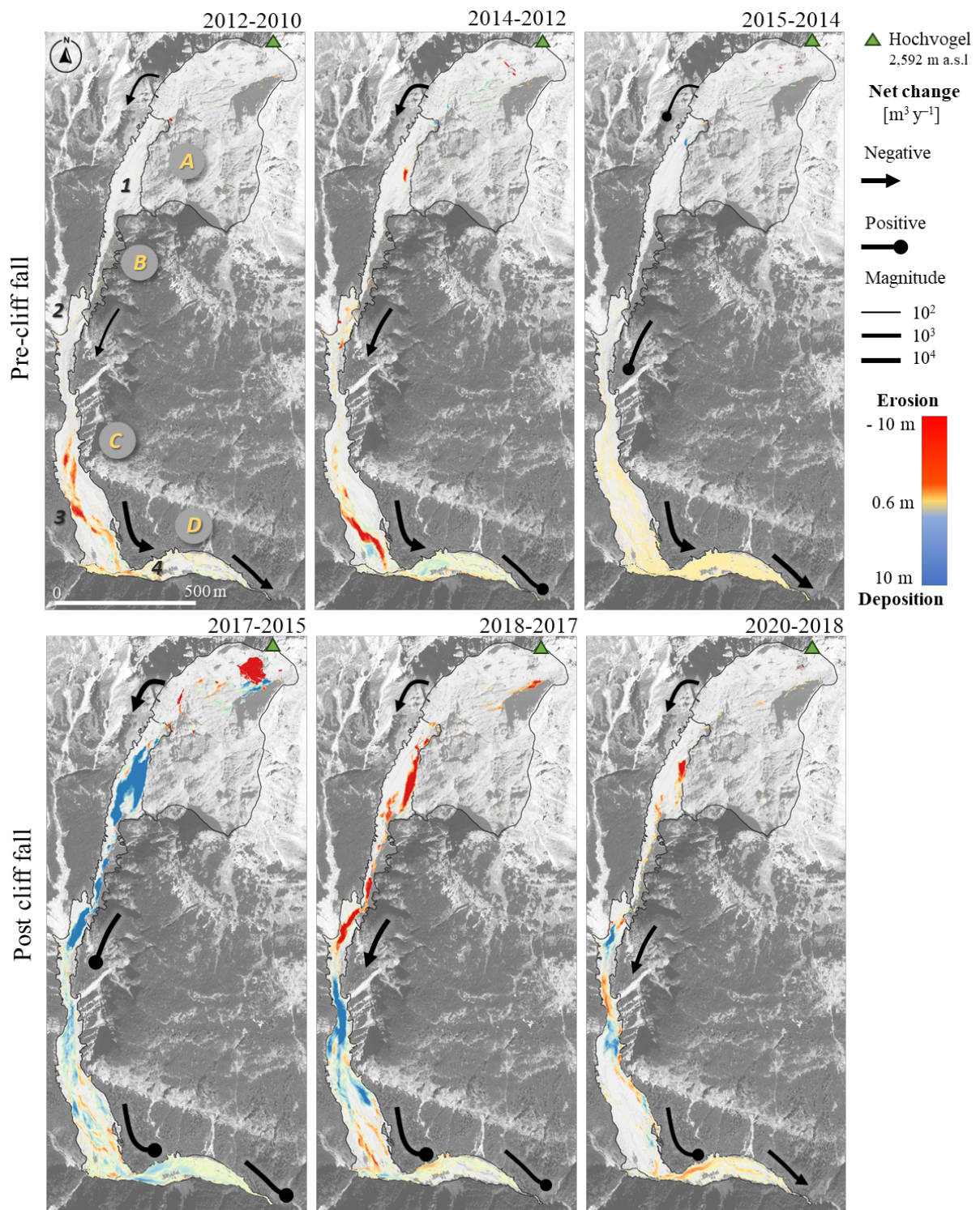
### **5.1. Validity of measurements**

The main drawbacks of the presented measurements are related to (i) the nature of the nadir view aerial imagery  
450 acquisition that limits the representation of steep topography and (ii) the scarcity of seismic stations around the Hochvogel summit that challenge the identification of small-size rockfall volumes, constraining the measurements to high-magnitude events where seismic signals are more pronounced.

Considering the inhomogeneity of the aerial imagery, the quantitative data described above are comparable to  
455 other published results obtained by digital photogrammetry (e.g., Kaufmann and Ladstädter, 2003; Schiefer and Gilbert, 2007; Marzolf and Poesen, 2009; Fabris and Pesci, 2009; Micheletti et al., 2015; Hilger and Beylich, 2018; Geissler et al., 2021). The authors acknowledge the limitations of aerial imagery to depict vertical surfaces and in particular negative vertical surfaces. Nevertheless, the proposed workflow resulted in consistent landscape representations through time, evidenced by topographic profiles extracted from the DSM and volume calculation  
460 of the 2016 cliff fall using all possible DSM combinations (Table 6 supplementary material). Additionally, the



back calculation of the failed volumes from the seismic signals of regional stations (Sec. 4.1.) is in the range of the photogrammetrically determined volumes, thus supporting the results via a second methodological approach.



465 **Figure 7.** Time-series of spatial distribution of erosional (red) and depositional (blue) areas with black arrows as an  
 466 indication of sediment continuity based on the net changes. (A) rockface (B) upper channelized debris flow channel,  
 467 (C) widened dispersed debris flow channel, and (D) outlet to the Jochbach river. (1), (2), (3), and (4) mark the position  
 468 of morphological blockages corresponding to slope changes that promotes deposition thus attenuation in the sediment  
 469 flux.

470

Even though we followed a very conservative approach, possible overestimations of the volumes are expected, particularly for the rockface where complex topography predominates. When visualizing the point clouds, it is possible to perceive the dense point cloud on the horizontal surfaces, but little to no points on vertical and pseudo-vertical surfaces for some of the datasets (e.g., 2015 dataset). Additionally, even if the vertical sides are completely depicted, the gridded component of the analysis poorly represents the vertical topography. Nevertheless, poorly represented areas are excluded from the DSMs used for the calculation of topographic change. On the other hand, the results on the northern slope (Figure 5a), often acquired under poorer illumination conditions, are prone to higher uncertainty (0.6 to 1.2 m). The proposed workflow optimizes the relative uncertainty in the elevation component for each dataset and assesses systematic errors minimized by a spatially uniform critical threshold, but additional research is needed to better estimate the spatial distribution of random errors and proxies that leads to the quantification of a spatially variable uncertainty (Wheaton et al., 2010). Therefore, the segmentation of the DoDs was designed to filter topographic changes at each landscape compartment considering the stated data limitations. Lower uncertainty (between 0.1 to 0.3 m) is achieved at the widened dispersed debris flow channel and outlet due to more favorable geometry for the photogrammetric reconstruction., i.e., the perpendicular surface to the nadir-view which corresponds to a lower slope angle to flat topography. In spite of the discussed drawbacks, the presented workflow aims for an efficient and fast calculation of volumetric changes foreseen by the usage of aerial imagery for the early detection of future hazardous areas over wide extents or multiple basins in the context of a fast-changing climate and landscape.

The temporal resolution from large-format digital aerial surveys limits the quantification of single events, thus, the analysis of seismic datasets complements the photogrammetric record by deciphering the coalescence of events. The energy released by the rockfalls associated with the 2016 cliff fall was sufficient to be recorded despite the distance of the seismic stations (the closest station located at 11 km); therefore, we elucidate the multi-stage detachment of possibly 6 events with exact timing (3 block falls followed by 3 cliff falls). Contrary, the energy released by individual debris flows event is considerably less, thus challenging the usage of the current seismic network. Note that the latest three seismic events identified as rockfalls show clear evidence of a source located close to the Hochvogel rock failure, while the first three events are harder to constrain due to their smaller amplitude (Figure 8a,b and c supplementary material). Nevertheless, these also show the same intensity-distance decay and signal arrival time patterns and can therefore be considered. Additionally, the respective sub-event's percentage of the total volume is very similar for the stations OBER, RETA, DAVA, MOTA and A307A (Figure 7 and Table 13 supplementary material). The stations PART and ZUGS must be excluded due to their bad signal-to-noise ratio in the relevant frequency band. For a fall height of 60 m, the volume estimated from the seismic signal at OBER is 20 % lower than that estimated photogrammetrically, but the seismic method neglects detachments that are too small to be recorded by the distant broadband sensor, detachments from the same source area but not belonging to the 3-day event, and energy that gets lost due to fragmentation of the failed mass. The other stations further away underestimate the volume due to stronger signal damping, distortion and worse coupling compared to the closest station OBER.

## 5.2. Rockfall activity as landscape re-shaping mechanism

510 Bi-annual rockwall retreat rates for the five years prior to the cliff fall averaged  $6.5 \text{ mm y}^{-1}$ , slightly exceeding  
short-term ( $< 10$  years) rock wall retreats for limestones (Draebing et al., 2022). The maximum pre-cliff fall  
rockwall retreat corresponds to  $9.5 \text{ mm y}^{-1}$  between 2012 and 2014. The rockwall retreat rates are consistent with  
previous findings of enhanced rockfall activity for carbonate cliffs (Krautblatter et al., 2012). The (multi-) annual  
515 erosion across the rockface slope in the years prior to the cliff fall might reveal signs of alert. Close-up  
observations of the area of the cliff failure evidence block fall and boulder fall at the base of the failure with  
volumes of  $1.71 (\pm 0.005) * 10^3 \text{ m}^3$  and  $1.05 (\pm 0.003) * 10^3 \text{ m}^3$  in 2012-2014 and  $2.91 (\pm 0.01) * 10^2 \text{ m}^3$  in 2014-2015  
reflecting a main deformation area (Kromer et al., 2018). The cliff fall resulted in the rockwall retreat of  $390 \text{ mm}$   
 $\text{y}^{-1}$  between 2015 and 2017 increasing the mean steepness of the rockface by 1%. The consecutive detachment of  
520 at least 6 blockfalls over 3 days follows an increase in magnitude from  $10^3 \text{ m}^3$  to  $10^4 \text{ m}^3$  previously suggested by  
other studies (e.g., Kromer et al., 2017; Rosser et al., 2007; Abellán et al., 2009; Benjamin et al., 2020), and  
paramount for the understanding of cascading risk in alpine regions.

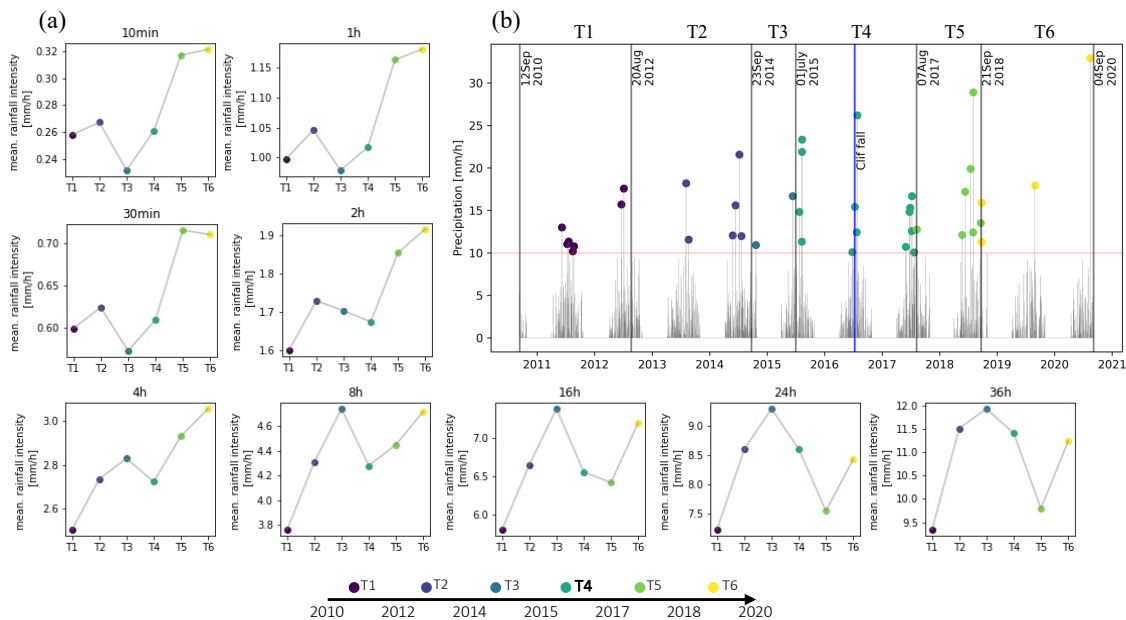
Despite of the greater distance between the Hochvogel summit and the seismic stations used to characterize the  
525 2016 cliff fall compared to the original source (Le Roy et al., 2019), the energy released by the 6 sub-events was  
sufficient to record and discriminate them. Regardless of the high temporal resolution achieved with the seismic  
analysis compared to the photogrammetric records, the triggering mechanism for this multi-stage event is hard to  
constrain because of the lack of high-resolution climatic datasets at local scales. Among common rockfall  
triggering factors are precipitation and cyclic thermal stressing (Dietze et al., 2017b, 2021). Climatic records from  
530 the surroundings of the Hochvogel (Station located at Obersdorf) showed that the multi-stage event is preceded  
by a phase of several dry and hot summer days. In the night before the first block fall, minor amounts of rain have  
been recorded, but the three final cliff falls on July 11<sup>th</sup> are preceded by more intense rainfall of up to  $1.4 \text{ mm}/10$   
min with a time lag of less than 1 h (Figure 4c). Also, all recorded events happened during the morning and  
evening hours where a strong thermal gradient might have an influence on the stressing of the rock mass (Dietze  
535 et al., 2017b, 2021). Contrary to rockfall observations from high temporal monitoring of cliff evolution (Williams  
et al., 2019), the sub-events prior to the cliff fall are unlikely to follow a pattern of increasing frequency and  
volumes through time.

## 5.3. Mechanism of sediment delivery continuity under a system disturbance.

Typical geomorphic responses to disturbances include increased rates of sediment remobilization, transport and  
540 deposition (e.g., Owens et al., 2010; Bennett et al., 2013; Baer et al., 2017; Frank et al., 2019; Savi et al., 2023). -  
However, sediment export from the basin rarely reflects changes in sediment transfer within a catchment (Walling,  
1983; Walling and Collins, 2008; Burt and Allison, 2010) due to the high variability in time and scale of sediment  
morphodynamics. The catchment sediment budgets at the Hochvogel clearly suggest a perturbation in the system  
with at least a year reaction time evidenced in the shift between predominant deposition to increased erosion. The  
545 segregated sediment budget (Figure 6a) and the time series of spatial distribution of erosion and deposition (Figure  
7) provide insights on the predominant processes controlling the transfer of sediment within the slope. Conceptual

models on sediment cascades on landslide-prone catchments propose the temporal accumulation on slopes from landslide deposits that become available for further remobilization (Harvey, 2001). Sediment transport depends on hydrological conditions and sediment supply, while superimposed debris flows are a common and efficient mechanism of sediment transport (Benda and Dunne, 1997; Schwab et al., 2008; Bennett et al., 2013; Clapuyt et al., 2019). The surrounding of the Hochvogel displays an increased mean seasonal (April-November) rainfall intensity over the last decades for events with durations of less than 4 hours (Figure 8a). However, the number of days with precipitation exceeding rainfall thresholds reported in the literature for sediment transport (2.2 mm/10 min) and debris flows initiation (3.8 to 9.6 mm/10 min and 5 and 15 mm/h) (Hürlimann et al., 2019) exhibit no significant difference between the periods before and after the cliff fall suggesting no clear rainfall related trigger for the massive sediment redistribution after the cliff fall. Note the increased number of days with exceeding rainfall thresholds of 10mm/h, 3.8 mm/10min, and 9.6mm/10min for the time interval when the cliff fall occurred (Figure 8b. 2015-2017: T4) while a depositional regime characterizes the sediment dynamics during this period as a consequence of the massive sediment production from the cliff fall. Conversely, the number of days exceeding common rainfall thresholds for the time interval between 2017-2018 (T5 in Figure 8b) characterized by massive sediment redistribution within the catchment is similar to pre-cliff fall intervals. These findings agree with previous studies where no clear rainfall trigger was found for massive sediment redistribution (e.g., Bennett et al., 2013; Frank et al., 2019). Numerical modeling demonstrate that both antecedent moisture and sediment storage are key for debris flow prediction (Bennett et al., 2013, 2014).

565



570

**Figure 8. Intensity-duration and frequency analysis for a diversity of rainfall events measured at the precipitation station 6290-Hinterhornbach/AUS. Data basis: Deutscher Wetterdienst, cumulative sum over individual values. The storm analysis was performed by splitting the rainfall datasets by the acquisition dates of the aerial imagery being: T1, T2, and T3, the years before the cliff fall plotted in blue shades; T4 the mean rainfall after, during and one year after the cliff fall in light green; and T5 and T6 the time intervals with increased erosion in light green and yellow. a) mean rainfall intensity with a diversity of durations for the analysed time intervals. b) discrete daily precipitation between 2011 and 2021. Dots highlight days with rainfall intensity exceeding 10 mm/h.**

575

Sediment transport by channelized debris flows is a common process in the studied catchment before the cliff fall event but is spatially confined to the widened dispersed debris flow channel (Figure 7, 2010-2012, 2012-2014). Similarly, to the Dolomite region (Italian Alps), debris flow initiation occurred at the outlet of a small basin where concentrated overland flow feeds an ephemeral channel that incised slope deposits (Berti and Simoni, 2005).

580 Monitoring at the Swiss Alps suggests increased debris flow activity after a sudden sediment input from a rock avalanche or large landslide (Bennett et al., 2014; Baer et al., 2017; Frank et al., 2019). A numerical modeling by Bennett et al. (2014), calibrated for a debris flow-prone catchment enhanced the key role of sediment supply in debris flow formation even in erosive catchments. Even if the model results in transport-limited behavior for more than half of the time, the supply-limited condition in the debris flow channel results in highly nonlinear sediment

585 discharge as a function of runoff. The material detached by the cliff fall entrained older deposits at the upper channelized erosive debris channel, which we traced back to 1945 by the visual inspection of historical aerial imagery, increasing the amount of transported sediment downslope. Despite this, inferred trajectories of sediment waves from the visual inspection of temporal series of orthophotos, most likely coalescent debris flows, and bulk erosion patterns, evidence short travel distances (<500 m), promoting the sediment transfer within the slope

590 morphodynamic zones but rarely reaching the outlet. Multiple debris flow events were visually identified on the orthophotos based on differences in color and granulometry, but a complete separation remains challenging. Recent debris flow numerical models emphasize the importance of the topography on their motion, the role of retention basins and memory effects for the acceleration-deceleration stage of the flow (Qiao et al., 2023), and the spatial distribution of eroded volumes (Haas et al., 2020). The sediment storages and sinks (marked as (1), (2),

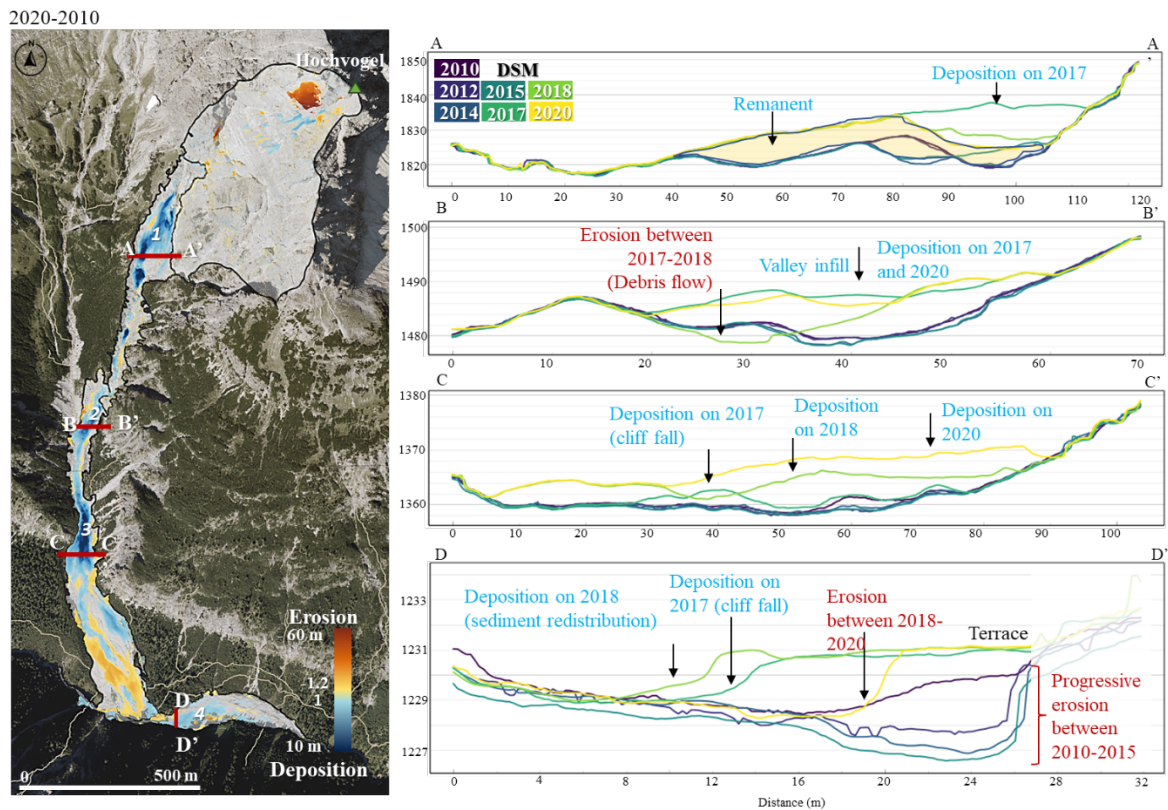
595 (3), and (4) in Figure 7) at our study catchment spatially correspond to slope changes which might decrease flow energy and thus debris flow travel distances. The enhanced accumulation in this region is visible in the decadal topographic change in Figure 9-left. Currently, these areas with at least 10 m of recently cumulated sediment remain prone to mobilization possibly extending the system relaxation times (Heckmann and Schwanghart, 2013).

600 Numerical models assessing the role of precipitation changes, runoff, and air temperature on sediment yield and debris flow activity suggest a reduction in both sediment supply and debris flow for the used climatic predictions. Additionally, the models identified sediment input into the sediment cascades as a key parameter for debris flow activity (Hirschberg et al., 2021). The presented results exemplify how sediment input produced by a cliff fall resulted in the sediment continuity from the rockface to the outlet, however, the degree of continuity measured as

605 the negative net change, decreased considerably during the four years after the cliff fall (Figure 6 right). The results align with recent observations on the key role of sediment supply in landscape connectivity (Heckmann and Schwanghart, 2013), sediment continuity (Joyce et al., 2018), and debris flow occurrences (Bennett et al., 2013; Baer et al., 2017; Hirschberg et al., 2021; Battista et al., 2022). The remaining key questions deal with the interactions of sediment supply and hydrological conditions and the timing and mechanisms, e.g., sediment

610 exhaustion, required to reestablish the pre-event morphodynamics where the rockface is decoupled from the fluvial system. Predictions on the sediment cascade at the Hochvogel required a deeper understanding of the rockfall triggering factors and rates of sediment production, currently the object of research. On the other hand, sediment storages resulting from geomorphic processes such as high magnitude slope instability and paraglacial and glacier sediment storages, are often landforms decoupled from the present-day geomorphic process, therefore,

615 studying the conditions that lead to increased sediment transport and reconnection of those systems support the prediction of geomorphic impact under a changing climate.



620 **Figure 9. Left. Decadal topographic change. Right. Topographic profiles at retention basins. Left: Cumulative**  
**topographic changes between 2010 and 2020. Dark blue areas indicate remaining sediment deposits with more than**  
**10m in elevation. Profile A-A' shows the formation of a depositional geomorph (sediment talus) which is partially**  
**eroded in the next few years. Blue polygon highlights the remanent sediment wedge with a depth of c.a. 10 m. Profile**  
**B-B' is located in the transfer zone between the Weittal valley and the lower valley. The confined valley is filled with**  
**sediment transferred from the cliff fall in 2017, partially eroded between 2017-2018, and filled again with sediment**  
**produced by secondary rockfalls and debris flows in 2020. Profile C-C' exhibits the dynamic of the confined fan apex**  
**which is slightly affected by the primary sediment produced during the cliff event but heavily impacted by the**  
**cascades. Progressive aggradation since 2017 evidenced the sediment waves in the system. Profile D-D', shows the**  
**formation and current erosion of a terrace formed as a result of the sediment that reached the outlet of the**  
**Wildenbach catchment. An initial sediment wave blocked partially the Jochbach river by c.a. 3 m of sediment.**  
**Additional sediment was annexed to the terrace in 2018. Currently, a remnant of 3 m. width is observed, less than**  
**half of the original terrace.**

## 6. Conclusions

The combination of seismic information and temporal series of high-resolution wide-extent true-orthophotos and  
 635 DSMs provides an accurate assessment of the temporal and special evolution of rockfalls and the subsequent  
 massive sediment redistribution. A multi-stage detachment of more than 130,000 m<sup>3</sup> in the Hochvogel summit,  
 northern calcareous alps (DE/AT), was responsible for the production of 97% of the total sediment eroded between  
 2010 and 2020. We identified a significant disproportion in the contribution of rockfall magnitudes for the four  
 slopes that constitute the summit with predominance of debris falls for the northern and western slopes, while the  
 640 southeastern slope has a large proportion of boulder fall, thus, increased hazard. The seismic analysis revealed  
 consecutive blockfalls with increased magnitude from 10<sup>3</sup> to 10<sup>4</sup> m<sup>3</sup> in a time period of 3 days during the summer  
 of 2016, strongly increasing the rockfall risk in the area. Therefore, these results underscore the need of monitoring

alpine slopes to better assess possible increased rockfall activity that leads to safety concerns. We suggest the integration of wide-extend photogrammetric datasets in future alpine early warning system.

645

The time series of spatial distribution of differences of DSM and differentiated geomorphic sediment budgets contributes to a better understanding of the complex nature and feedback of cascading processes. The alpine catchment quickly responded to the cliff fall within 0 to 4 years, resulting in massive sediment redistribution within the catchment and reduction in sediment delivery to the outlet. This, in turn, modified the fluvial response at the catchment outlet. Sediment continuity/transfer within the hillslope was rapidly recovered two years following the cliff fall. The recovered sediment flux mobilizes sediment along the geomorphic subsystems; however, the sediment waves were inefficient in delivering sediment to the catchment outlet. Relaxation times are expected beyond 10 years given that the latest observations (2020) still revealed perturbation in the system and the deposition of up to 10 m of sediment at the upper channelized debris flow which serves as a sediment input for future debris flows.

650

655

The results present the first step towards a better understanding, prediction, and early warning of alpine natural hazards under expected extreme climatic conditions. The ongoing interdisciplinary AlpSenseRely project aims to integrate high-resolution multi-scale, multi-temporal remote sensing data (Large format digital aerial photogrammetry and UAV) for an accurate quantification of temporal and spatial changes in alpine geomorphic systems.

660

#### **Data Availability**

The original aerial imagery is available at Landesamt für Digitalisierung, Breitband und Vermessung (LDBV), Bundesamt für Eich- und Vermessungswesen (BEV), and 3D RealityMaps GmbH upon request. Precipitation data is freely available at the Geoportal from the Deutscher Wetterdienst (<https://dwd-geoportal.de/>). Seismic data is freely available at reported sources in the supplementary material. The presented results are available for visualization online at <https://og.realitymaps.de/AlpSenseRely/>.

665

#### **Author contributions**

N.B. wrote the manuscript with contributions from J.L.

670

N.B. developed the topographic time series workflow, analyzed the data and compiled results

J.L. calculated seismic volumes

J.J. created DSM and orthophotos from digital aerial imagery

M.D. verified and advised on the implementation of the seismic volume's calculation

U.M, F.S and M.K provided guidance and funding

675

All authors checked and revised the text and the figures of the manuscript and contributed to the ideas developed in this study.

#### **Competing interests**

An author is a member of the editorial board of the journal Earth Surface Dynamics. The peer-review process was guided by an independent editor, and the authors have also no other competing interest to declare.

680

#### **Acknowledgments**

We thank the Land Tyrol and particularly Mag. Thomas Figl for the open sharing of the pictures taken during the aerial inspection of the Hochvogel before the cliff fall which helped us to better picture the magnitude of the

detachment, the Landslide research group at TUM for the fieldwork support during the UAV acquisitions, particularly to Andreas Dietrich for the UAV acquisition on 2017. The publication of this work was financially supported by the Ludwig-Maximilians-University (LMU) through the ‘Open Access Publishing’ program. We are indebted to Peter Mederer for his contribution to the early developments of the 3D-coregistration python workflow during his internship at 3D RealityMaps GmbH, and the colleagues at 3D RealityMaps GmbH, Munich for the outstanding support with the implementation of the 3D models used for visualization, visual interpretation, and figures. We would like to thank the anonymous reviewers and Dr. David Mair for the time devoted to the manuscript and special thanks to Dr. Georgina Bennett for the constructive comments to improve the quality of the manuscript.

### Financial support

This research was funded by the Bavarian State Ministry of the Environment and Consumer Protection (StMUV) in the framework of the project “AlpSenseRely” Alpine remote sensing of climate-induced natural hazards: Reliability of multi-method hazard prediction in a changing climate (Teilprojekt for LMU TUSO1UFS-77318). Initial datasets were acquired during the project ‘AlpSenseBench’ Alpine remote sensing of climate-induced natural hazards funded by the Bavarian State Ministry for Economic Affairs, Regional Development and Energy (StMWI) (grant no. 45-6723a/15/2).

### References

- Abellán, A., Jaboyedoff, M., Oppikofer, T., and Vilaplana, J. M.: Detection of millimetric deformation using a terrestrial laser scanner: experiment and application to a rockfall event, *Nat Hazard Earth Sys*, 9, 365–372, <https://doi.org/10.5194/nhess-9-365-2009>, 2009.
- Anderson, S. W.: Uncertainty in quantitative analyses of topographic change: error propagation and the role of thresholding, *Earth Surf Processes*, 44, 1015–1033, <https://doi.org/10.1002/esp.4551>, 2019.
- Baer, P., Huggel, C., McArdell, B. W., and Frank, F.: Changing debris flow activity after sudden sediment input: a case study from the Swiss Alps, *Geology Today*, 33, 216–223, <https://doi.org/10.1111/gto.12211>, 2017.
- Battista, G., Schlunegger, F., Burlando, P., and Molnar, P.: Sediment Supply Effects in Hydrology-Sediment Modeling of an Alpine Basin, *Water Resour Res*, 58, <https://doi.org/10.1029/2020wr029408>, 2022.
- Becht, M., Haas, F., Heckmann, T., and Wichmann, V.: A new modelling approach to delineate the spatial extent of alpine sediment cascades, *Geomorphology*, 111, 70–78, <https://doi.org/10.1016/j.geomorph.2008.04.028>, 2009.
- Benda, L. E. and Dunne, T.: Stochastic Forcing of Sediment Routing and Storage in Channel Networks, *Water Resources Research*, 33, 2865–2880, <https://doi.org/10.1029/97wr02387>, 1997.
- Benjamin, J., Rosser, N. J., and Brain, M. J.: Emergent characteristics of rockfall inventories captured at a regional scale, *Earth Surf Processes*, 45, 2773–2787, <https://doi.org/10.1002/esp.4929>, 2020.
- Bennett, G. L., Molnar, P., Eisenbeiss, H., and McArdell, B. W.: Erosional power in the Swiss Alps: characterization of slope failure in the Illgraben, *Earth Surf. Process. Landforms*, 37, 1627–1640, <https://doi.org/10.1002/esp.3263>, 2012.
- Bennett, G. L., Molnar, P., McArdell, B. W., Schlunegger, F., and Burlando, P.: Patterns and controls of sediment production, transfer and yield in the Illgraben, *Geomorphology*, 188, 68–82, <https://doi.org/10.1016/j.geomorph.2012.11.029>, 2013.



- Bennett, G. L., Molnar, P., McArdell, B. W., and Burlando, P.: A probabilistic sediment cascade model of sediment transfer in the Illgraben, *Water Resour Res*, 50, 1225–1244, <https://doi.org/10.1002/2013wr013806>, 2014.
- 725
- Berger, C., McArdell, B. W., and Schlunegger, F.: Sediment transfer patterns at the Illgraben catchment, Switzerland: Implications for the time scales of debris flow activities, *Geomorphology*, 125, 421–432, <https://doi.org/10.1016/j.geomorph.2010.10.019>, 2011.
- Berti, M. and Simoni, A.: Experimental evidences and numerical modelling of debris flow initiated by channel runoff, *Landslides*, 2, 171–182, <https://doi.org/10.1007/s10346-005-0062-4>, 2005.
- 730
- Bollschweiler, M. and Stoffel, M.: Changes and trends in debris-flow frequency since AD 1850: Results from the Swiss Alps, *Holocene*, 20, 907–916, <https://doi.org/10.1177/0959683610365942>, 2010.
- Borselli, L., Cassi, P., and Torri, D.: Prolegomena to sediment and flow connectivity in the landscape: A GIS and field numerical assessment, *CATENA*, 75, 268–277, <https://doi.org/10.1016/j.catena.2008.07.006>, 2008.
- 735
- Bracken, L. J., Turnbull, L., Wainwright, J., and Bogaart, P.: Sediment connectivity: a framework for understanding sediment transfer at multiple scales, *Earth Surf Processes*, 40, 177–188, <https://doi.org/10.1002/esp.3635>, 2015.
- Brown, A. G., Carey, C., Erkens, G., Fuchs, M., Hoffmann, T., Macaire, J.-J., Moldenhauer, K.-M., and Walling, D. E.: From sedimentary records to sediment budgets: Multiple approaches to catchment sediment flux, *Geomorphology*, 108, 35–47, <https://doi.org/10.1016/j.geomorph.2008.01.021>, 2009.
- 740
- Burt, T. P. and Allison, R. J.: *Sediment Cascades. An Integrated Approach*, First edition., John Wiley & Sons, Ltd, 2010.
- Clapuyt, F., Vanacker, V., Christl, M., Oost, K. V., and Schlunegger, F.: Spatio-temporal dynamics of sediment transfer systems in landslide-prone Alpine catchments, *Solid Earth*, 10, 1489–1503, <https://doi.org/10.5194/se-10-1489-2019>, 2019.
- 745
- CloudCompare v2.0: A software for processing and comparing 3D point clouds: <http://www.cloudcompare.com>.
- DAV, D.: Neue Felsstürze vom Hochvogel ins Weittal, Juli 2016 | Neue Felsstürze vom Hochvogel ins Weittal, 2016.
- DAV, D.: *Chronik - Sperrung des Bäumenheimer Weges, Sperrung Bäumenheimer Weg*, 2017.
- 750
- Dietrich, W. E., Dunne, T., Humphrey, N. F., and Reid, L. M.: Construction of sediment budgets for drainage basins, in: *Construction of sediment budgets for drainage basins*, vol. 141, 5–23, 1982.
- Dietze, M., Mohadjer, S., Turowski, J. M., Ehlers, T. A., and Hovius, N.: Seismic monitoring of small alpine rockfalls – validity, precision and limitations, *Earth Surf Dynam*, 5, 653–668, <https://doi.org/10.5194/esurf-5-653-2017>, 2017a.
- 755
- Dietze, M., Turowski, J. M., Cook, K. L., and Hovius, N.: Spatiotemporal patterns, triggers and anatomies of seismically detected rockfalls, *Earth Surf Dynam*, 5, 757–779, <https://doi.org/10.5194/esurf-5-757-2017>, 2017b.
- Dietze, M., Krautblatter, M., Illien, L., and Hovius, N.: Seismic constraints on rock damaging related to a failing mountain peak: the Hochvogel, Allgäu, *Earth Surf. Process. Landforms*, 46, 417–429, <https://doi.org/10.1002/esp.5034>, 2021.
- 760
- Draebing, D., Mayer, T., Jacobs, B., and McColl, S. T.: Alpine rockwall erosion patterns follow elevation-dependent climate trajectories, *Commun Earth Environ*, 3, 21, <https://doi.org/10.1038/s43247-022-00348-2>, 2022.

- 765 Dussauge-Peisser, C., Helmstetter, A., Grasso, J.-R., Hantz, D., Desvarreux, P., Jeannin, M., and Giraud, A.: Probabilistic approach to rock fall hazard assessment: potential of historical data analysis, *Nat Hazard Earth Sys*, 2, 15–26, <https://doi.org/10.5194/nhess-2-15-2002>, 2002.
- Eltner, A. and Sofia, G.: Structure from motion photogrammetric technique, in: *Developments in Earth surface process*, vol. 23, edited by: Tarolli, P. and Mudd, S. M., 1–24, <https://doi.org/10.1016/b978-0-444-64177-9.00001-1>, 2020.
- 770 Erismann, T. H. and Abele, G.: *Dynamics of Rockslides and Rockfalls*, Springer Science & Business Media, Heidelberg, 2001.
- Fabris, M. and Pesci, A.: Automated DEM extraction in digital aerial photogrammetry: precisions and validation for mass movement monitoring, *Ann Geophys-italy*, 48, <https://doi.org/10.4401/ag-3247>, 2009.
- 775 Fawcett, D., Blanco-Sacristán, J., and Benaud, P.: Two decades of digital photogrammetry: Revisiting Chandler’s 1999 paper on “Effective application of automated digital photogrammetry for geomorphological research” – a synthesis, *Prog Phys Geogr Earth Environ*, 43, 299–312, <https://doi.org/10.1177/0309133319832863>, 2019.
- Fischer, L., Purves, R. S., Huggel, C., Noetzli, J., and Haerberli, W.: On the influence of topographic, geological and cryospheric factors on rock avalanches and rockfalls in high-mountain areas, *Nat Hazard Earth Sys*, 12, 241–254, <https://doi.org/10.5194/nhess-12-241-2012>, 2012.
- 780 Frank, F., Huggel, C., McArdell, B. W., and Vieli, A.: Landslides and increased debris-flow activity: A systematic comparison of six catchments in Switzerland, *Earth Surf Processes*, 44, 699–712, <https://doi.org/10.1002/esp.4524>, 2019.
- Fryirs, K.: (Dis)Connectivity in catchment sediment cascades: a fresh look at the sediment delivery problem, *Earth Surf Processes*, 38, 30–46, <https://doi.org/10.1002/esp.3242>, 2013.
- 785 Fuchs, F., Lenhardt, W., Bokelmann, G., and Group, the A. W.: Seismic detection of rockslides at regional scale: examples from the Eastern Alps and feasibility of kurtosis-based event location, *Earth Surf Dynam*, 6, 955–970, <https://doi.org/10.5194/esurf-6-955-2018>, 2018.
- 790 Geissler, J., Mayer, C., Jubanski, J., Münzer, U., and Siegert, F.: Analyzing glacier retreat and mass balances using aerial and UAV photogrammetry in the Ötztal Alps, Austria, *Cryosphere*, 15, 3699–3717, <https://doi.org/10.5194/tc-15-3699-2021>, 2021.
- Gregory, K. J. and Lewin, J.: *The Basics of Geomorphology: Key Concepts*, <https://doi.org/10.4135/9781473909984>, 2014.
- 795 Guerin, A., Ravanel, L., Matasci, B., Jaboyedoff, M., and Deline, P.: The three-stage rock failure dynamics of the Drus (Mont Blanc massif, France) since the June 2005 large event, *Sci Rep-uk*, 10, 17330, <https://doi.org/10.1038/s41598-020-74162-1>, 2020.
- Haala, N. and Rothermel, M.: Dense Multi-Stereo Matching for High Quality Digital Elevation Models, *Photogrammetrie - Fernerkundung - Geoinformation*, 2012, 331–343, <https://doi.org/10.1127/1432-8364/2012/0121>, 2012.
- 800 Haas, T. de, Nijland, W., Jong, S. M. de, and McArdell, B. W.: How memory effects, check dams, and channel geometry control erosion and deposition by debris flows, *Sci. Rep.*, 10, 14024, <https://doi.org/10.1038/s41598-020-71016-8>, 2020.
- Hantz, D., Corominas, J., Crosta, G. B., and Jaboyedoff, M.: Definitions and Concepts for Quantitative Rockfall Hazard and Risk Analysis, *Geosciences*, 11, 158, <https://doi.org/10.3390/geosciences11040158>, 2021.

- 805 Harvey, A. M.: Coupling between hillslopes and channels in upland fluvial systems: implications for landscape sensitivity, illustrated from the Howgill Fells, northwest England, *CATENA*, 42, 225–250, [https://doi.org/10.1016/s0341-8162\(00\)00139-9](https://doi.org/10.1016/s0341-8162(00)00139-9), 2001.
- Heckmann, T. and Schwanghart, W.: Geomorphic coupling and sediment connectivity in an alpine catchment — Exploring sediment cascades using graph theory, *Geomorphology*, 182, 89–103, <https://doi.org/10.1016/j.geomorph.2012.10.033>, 2013.
- 810 Heckmann, T., Bimböse, M., Krautblatter, M., Haas, F., Becht, M., and Morche, D.: From geotechnical analysis to quantification and modelling using LiDAR data: a study on rockfall in the Reintal catchment, Bavarian Alps, Germany, *Earth Surf Processes*, 37, 119–133, <https://doi.org/10.1002/esp.2250>, 2012.
- 815 Heckmann, T., Hilger, L., Vehling, L., and Becht, M.: Integrating field measurements, a geomorphological map and stochastic modelling to estimate the spatially distributed rockfall sediment budget of the Upper Kaunertal, Austrian Central Alps, *Geomorphology*, 260, 16–31, <https://doi.org/10.1016/j.geomorph.2015.07.003>, 2016.
- Heißel, G. and Figl, T.: Stellungnahme der Amtssachverständigen für Geologie, Hydrogeologie und technische Geologie, sowie für den Schutz vor Erosion und vor alpinen geogenen Naturgefahren, 2017.
- 820 Hibert, C., Mangeney, A., Grandjean, G., and Shapiro, N. M.: Slope instabilities in Dolomieu crater, Réunion Island: From seismic signals to rockfall characteristics, *J Geophys Res Earth Surf*, 116, <https://doi.org/10.1029/2011jf002038>, 2011.
- Hilger, L. and Beylich, A. A.: Geomorphology of Proglacial Systems, Landform and Sediment Dynamics in Recently Deglaciated Alpine Landscapes, *Geogr Phys Environ*, 251–269, [https://doi.org/10.1007/978-3-319-94184-4\\_15](https://doi.org/10.1007/978-3-319-94184-4_15), 2018.
- 825 Hirschberg, J., Faticchi, S., Bennett, G. L., McArdell, B. W., Peleg, N., Lane, S. N., Schlunegger, F., and Molnar, P.: Climate Change Impacts on Sediment Yield and Debris-Flow Activity in an Alpine Catchment, *J. Geophys. Res.: Earth Surf.*, 126, <https://doi.org/10.1029/2020jf005739>, 2021.
- Hirschmüller, H.: Stereo Processing by Semiglobal Matching and Mutual Information, *Ieee T Pattern Anal*, 30, 328–341, <https://doi.org/10.1109/tpami.2007.1166>, 2008.
- 830 Hungr, O., McDougall, S., Wise, M., and Cullen, M.: Magnitude–frequency relationships of debris flows and debris avalanches in relation to slope relief, *Geomorphology*, 96, 355–365, <https://doi.org/10.1016/j.geomorph.2007.03.020>, 2008.
- Hürlimann, M., Rickenmann, D., Medina, V., and Bateman, A.: Evaluation of approaches to calculate debris-flow parameters for hazard assessment, *Eng Geol*, 102, 152–163, <https://doi.org/10.1016/j.enggeo.2008.03.012>, 2008.
- 835 Hürlimann, M., Coviello, V., Bel, C., Guo, X., Berti, M., Graf, C., Hübl, J., Miyata, S., Smith, J. B., and Yin, H.-Y.: Debris-flow monitoring and warning: review and examples, *Earth-sci Rev*, 199, 102981, <https://doi.org/10.1016/j.earscirev.2019.102981>, 2019.
- Jakob, M.: A size classification for debris flows, *Eng Geol*, 79, 151–161, <https://doi.org/10.1016/j.enggeo.2005.01.006>, 2005.
- 840 James, L. A., Hodgson, M. E., Ghoshal, S., and Latiolais, M. M.: Geomorphic change detection using historic maps and DEM differencing: The temporal dimension of geospatial analysis, *Geomorphology*, 137, 181–198, <https://doi.org/10.1016/j.geomorph.2010.10.039>, 2012.
- 845 Joyce, H. M., Hardy, R. J., Warburton, J., and Large, A. R. G.: Sediment continuity through the upland sediment cascade: geomorphic response of an upland river to an extreme flood event, *Geomorphology*, 317, 45–61, <https://doi.org/10.1016/j.geomorph.2018.05.002>, 2018.

- Kaufmann, V. and Ladstädter, R.: Quantitative analysis of rock glacier creep by means of digital photogrammetry using multi-temporal aerial photographs: Two case studies in the Austrian Alps, in: Proceedings of the 8th International Conference on Permafrost, 525–530, 2003.
- 850 Kazhdan, M., Chuang, M., Rusinkiewicz, S., and Hoppe, H.: Poisson Surface Reconstruction with Envelope Constraints, *Comput Graph Forum*, 39, 173–182, <https://doi.org/10.1111/cgf.14077>, 2020.
- Korup, O., Densmore, A. L., and Schlunegger, F.: The role of landslides in mountain range evolution, *Geomorphology*, 120, 77–90, <https://doi.org/10.1016/j.geomorph.2009.09.017>, 2010.
- 855 Krautblatter, M., Moser, M., Schrott, L., Wolf, J., and Morche, D.: Significance of rockfall magnitude and carbonate dissolution for rock slope erosion and geomorphic work on Alpine limestone cliffs (Reintal, German Alps), *Geomorphology*, 167, 21–34, <https://doi.org/10.1016/j.geomorph.2012.04.007>, 2012.
- Kromer, R., Lato, M., Hutchinson, D. J., Gauthier, D., and Edwards, T.: Managing rockfall risk through baseline monitoring of precursors using a terrestrial laser scanner, *Can Geotech J*, 54, 953–967, <https://doi.org/10.1139/cgj-2016-0178>, 2017.
- 860 Kromer, R. A., Rowe, E., Hutchinson, J., Lato, M., and Abellán, A.: Rockfall risk management using a pre-failure deformation database, *Landslides*, 15, 847–858, <https://doi.org/10.1007/s10346-017-0921-9>, 2018.
- Lacroix, P. and Helmstetter, A.: Location of Seismic Signals Associated with Microearthquakes and Rockfalls on the Séchilienne Landslide, French Alps Location of Seismic Signals Associated with Microearthquakes and Rockfalls on Séchilienne Landslide, *B Seismol Soc Am*, 101, 341–353, <https://doi.org/10.1785/0120100110>, 2011.
- 865 Leinauer, J., Jacobs, B., and Krautblatter, M.: Anticipating an imminent large rock slope failure at the Hochvogel (Allgäu Alps), *Geomechanics Tunn*, 13, 597–603, <https://doi.org/10.1002/geot.202000027>, 2020.
- Leinauer, J., Jacobs, B., and Krautblatter, M.: High alpine geotechnical real time monitoring and early warning at a large imminent rock slope failure (Hochvogel, GER/AUT), *Iop Conf Ser Earth Environ Sci*, 833, 012146, <https://doi.org/10.1088/1755-1315/833/1/012146>, 2021.
- 870 Le Roy, G., Helmstetter, A., Amitrano, D., Guyoton, F., and Roux-Mallouf, R. L.: Seismic Analysis of the Detachment and Impact Phases of a Rockfall and Application for Estimating Rockfall Volume and Free-Fall Height, *J Geophys Res Earth Surf*, 124, 2602–2622, <https://doi.org/10.1029/2019jf004999>, 2019 Manconi, A., Picozzi, M., Coviello, V., Santis, F. D., and Elia, L.: Real-time detection, location, and characterization of rockslides using broadband regional seismic networks, *Geophys Res Lett*, 43, 6960–6967, 875 <https://doi.org/10.1002/2016gl069572>, 2016.
- Marzollf, I. and Poesen, J.: The potential of 3D gully monitoring with GIS using high-resolution aerial photography and a digital photogrammetry system, *Geomorphology*, 111, 48–60, <https://doi.org/10.1016/j.geomorph.2008.05.047>, 2009.
- 880 McSaveney, M. J.: Recent rockfalls and rock avalanches in Mount Cook National Park, New Zealand, in: *Catastrophic Landslides Effects, occurrences and Mechanisms*, vol. XV, Geological Society of America, <https://doi.org/10.1130/reg15>, 2002.
- Mergili, M., Jaboyedoff, M., Pullarello, J., and Pudasaini, S. P.: Back calculation of the 2017 Piz Cengalo–Bondo landslide cascade with r.avaflow: what we can do and what we can learn, *Nat Hazard Earth Sys*, 20, 505–520, <https://doi.org/10.5194/nhess-20-505-2020>, 2020.
- 885 Micheletti, N., Lane, S. N., and Chandler, J. H.: Application of archival aerial photogrammetry to quantify climate forcing of alpine landscapes, *Photogrammetric Rec*, 30, 143–165, <https://doi.org/10.1111/phor.12099>, 2015.
- NNZ: Die Murgänge bei Bondo kosten rund 41 Millionen Franken, , 14th December, 2017.

- Owens, P. N., Peticrew, E. L., and Perk, M. van der: Sediment response to catchment disturbances, *J Soils Sediments*, 10, 591–596, <https://doi.org/10.1007/s11368-010-0235-1>, 2010.
- 890 Qiao, Z., Li, T., Simoni, A., Gregoretta, C., Bernard, M., Wu, S., Shen, W., and Berti, M.: Numerical modelling of an alpine debris flow by considering bed entrainment, *Front. Earth Sci.*, 10, 1059525, <https://doi.org/10.3389/feart.2022.1059525>, 2023.
- Rickenmann, D.: *Debris-flow Hazards and Related Phenomena*, Springer Praxis Books, 305–324, 895 [https://doi.org/10.1007/3-540-27129-5\\_13](https://doi.org/10.1007/3-540-27129-5_13), 2005.
- Riggs, H. C.: *Frequency Curves*, US Government Printing Office, 1968.
- Rosser, N., Lim, M., Petley, D., Dunning, S., and Allison, R.: Patterns of precursory rockfall prior to slope failure, *J Geophys Res Earth Surf* 2003 2012, 112, <https://doi.org/10.1029/2006jf000642>, 2007.
- Rothermel, Mathias., Wenzel, K., Fritsch, D., and Haala, N.: SURE: Photogrammetric surface reconstruction from imagery, in: *Proceedings LC3D Workshop*, 615–620, 2012.
- 900 Savi, S., Buter, A., Heckmann, T., Theule, J., Mao, L., and Comiti, F.: Multi-temporal analysis of morphological changes in an Alpine proglacial area and their effect on sediment transfer, *Catena*, 220, 106701, <https://doi.org/10.1016/j.catena.2022.106701>, 2023.
- Schiefer, E. and Gilbert, R.: Reconstructing morphometric change in a proglacial landscape using historical aerial photography and automated DEM generation, *Geomorphology*, 88, 167–178, 905 <https://doi.org/10.1016/j.geomorph.2006.11.003>, 2007.
- Schrott, L., Hufschmidt, G., Hankammer, M., Hoffmann, T., and Dikau, R.: Spatial distribution of sediment storage types and quantification of valley fill deposits in an alpine basin, Reintal, Bavarian Alps, Germany, *Geomorphology*, 55, 45–63, [https://doi.org/10.1016/s0169-555x\(03\)00131-4](https://doi.org/10.1016/s0169-555x(03)00131-4), 2003.
- 910 Schwab, M., Rieke-Zapp, D., Schneider, H., Liniger, M., and Schlunegger, F.: Landsliding and sediment flux in the Central Swiss Alps: A photogrammetric study of the Schimbrig landslide, Entlebuch, *Geomorphology*, 97, 392–406, <https://doi.org/10.1016/j.geomorph.2007.08.019>, 2008.
- Theler, D., Reynard, E., Lambiel, C., and Bardou, E.: The contribution of geomorphological mapping to sediment transfer evaluation in small alpine catchments, *Geomorphology*, 124, 113–123, 915 <https://doi.org/10.1016/j.geomorph.2010.03.006>, 2010.
- Thiele, S. T., Grose, L., Samsu, A., Micklethwaite, S., Vollgger, S. A., and Cruden, A. R.: Rapid, semi-automatic fracture and contact mapping for point clouds, images and geophysical data, *Solid Earth*, 8, 1241–1253, <https://doi.org/10.5194/se-8-1241-2017>, 2017.
- Tucker, G. E.: Drainage basin sensitivity to tectonic and climatic forcing: implications of a stochastic model for the role of entrainment and erosion thresholds, *Earth Surf Processes*, 29, 185–205, 920 <https://doi.org/10.1002/esp.1020>, 2004.
- Walling, D. E.: The sediment delivery problem, *J Hydrol*, 65, 209–237, [https://doi.org/10.1016/0022-1694\(83\)90217-2](https://doi.org/10.1016/0022-1694(83)90217-2), 1983.
- 925 Walling, D. E. and Collins, A. L.: The catchment sediment budget as a management tool, *Environ Sci Policy*, 11, 136–143, <https://doi.org/10.1016/j.envsci.2007.10.004>, 2008.
- Whalley, B.: *The mechanics of high-magnitude low-frequency rock failure and its importance in a mountainous area*, Reading Geographical Papers, 1974.
- Whalley, B.: *Rockfalls, Slope Instability*, Chapter 7, 1984.

- 930 Wheaton, J. M., Brasington, J., Darby, S. E., and Sear, D. A.: Accounting for uncertainty in DEMs from repeat topographic surveys: improved sediment budgets, *Earth Surf Processes*, 35, 136–156, <https://doi.org/10.1002/esp.1886>, 2010.
- Wichmann, V., Heckmann, T., Haas, F., and Becht, M.: A new modelling approach to delineate the spatial extent of alpine sediment cascades, *Geomorphology*, 111, 70–78, <https://doi.org/10.1016/j.geomorph.2008.04.028>, 2009.
- 935 Williams, J. G., Rosser, N. J., Hardy, R. J., and Brain, M. J.: The Importance of Monitoring Interval for Rockfall Magnitude-Frequency Estimation, *J Geophys Res Earth Surf*, 124, 2841–2853, <https://doi.org/10.1029/2019jf005225>, 2019.